

Spectroscopy in Helium Nanodroplets:  
Studying Relaxation Mechanisms  
in Nature's Most Fascinating Solvent

André Conjusteau

A DISSERTATION  
PRESENTED TO THE FACULTY  
OF PRINCETON UNIVERSITY  
IN CANDIDACY FOR THE DEGREE  
OF DOCTOR OF PHILOSOPHY  
  
RECOMMENDED FOR ACCEPTANCE  
BY THE DEPARTMENT OF CHEMISTRY

June 2002

© Copyright by André Conjusteau, 2002. All rights reserved.

# Abstract

Helium nanodroplet isolation spectroscopy has recently been developed to combine materials science and chemical dynamics studies at very low temperatures. The technique, a combination of beam and matrix isolation spectroscopy, shows great promise as a tool to study both the solvent properties of superfluid helium, and the relaxation dynamics of impurities embedded in it. This thesis presents two experiments designed to improve our understanding of solvation in superfluid helium.

Firstly, an experiment aimed at the formation *in situ* of radicals in helium nanodroplets has been performed. The photodissociation of NO<sub>2</sub> embedded in helium, using a high repetition rate narrowband U.V. laser, has been attempted. The experiment led to the surprising result that, even 2000 cm<sup>-1</sup> above the gas phase threshold, no signature of dissociation could be observed.

Secondly, a predicted limitation of a successful hydrodynamic model built to explain the increase in moment of inertia of molecules solvated in helium has been probed by microwave spectroscopy. The observation of the pure rotational spectra of isotopically substituted species (HCN/DCN, and CH<sub>3</sub>F/CD<sub>3</sub>F), leads to the unequivocal conclusion that the angular velocity of the rotor greatly affects its helium-induced increase in moment of inertia. For the cyanides, it has been found

that HCN, which is faster than DCN by 23% in the gas phase, sees its moment of inertia increase *less* (by 11%) than that of DCN. The fluorides show a different trend, which we believe is due to CD<sub>3</sub>F being a less anisotropic rotor than CH<sub>3</sub>F: the fastest of the two rotors, CH<sub>3</sub>F, sees a 10% *larger* increase in its moment of inertia.

# Acknowledgements

For those of you who will read the whole section only to get mad because you will find your name misspelled, just think of all those people who will read the whole section and won't even find their name because I forgot about them . . .

## The Princeton Chapter

First, let's give a good hand to the advisors, Giacinto Scoles and Kevin Lehmann. In the few instances where they actually agreed, it was just perfect. For all the "other times", it was great. I could say a lot of things to summarize five years of work in room 4, but sometimes less is better: Thanks.

Thanks to my reader, Pr. Marcel Nooijen, for giving me his million dollars' worth of "two cents". I *know* I can make the thesis better. Given infinite time, I would even learn to walk on water . . . Pr Charles Dismukes and Elmar Schreiber, the "others". Thanks for your help. I'm glad you accepted the (last minute) invitation.

A big hug for Ilse. Smiling all the time, always finding the right word to put a smile back on my face. You went pretty far beyond the call of duty after I left Princeton. Thanks a lot.

Thanks to all the Scolehmman Family members: Andrea and Carlo Callegari, Hemant Srivastava, Peter Engels, Gianni Pietraperzia, Susan Choi, Daniel Katz, Irene Reinhard, Iris Scheele, Pierre Çarçabal, Holger Lichau, Özgür Birer, John Higgins, James Reho, Matt Radcliff, Udo Merker, Paolo Moreschini, Roman Schmied, Peter Schwartz, Ying Hu, Adriana Gil, Fatih Danisman, Loredana Casalis, Nino Bracco, Jörg Libuda, Sean Wetterer, Dave Lavrich, Michael Gerstenberg, Becky Leung, Frank Schreiber, Peter Tarsa, John Dudek. Thanks to Michelle Silva for the ethylene experiment.

Karen Mink. Thank you so much for all the formal “...” related to the thesis and the organization of the FPO. It’s nice to have someone like you around, to show us that everything is nice and simple. You know everything, which makes life in Frick so much easier. Last time I checked, there was a sour cream donut waiting for you downstairs.

Larry ... Thanks for your patience, and for teaching me all that I know. And always remember: “Machining puts a smile on your face”! Phil Fairall, Kevin Wilkes, Janet Chrisman, Vicky Lloyd. Thanks!

## **The TechnoDudes**

Thanks to Norman Jarosik (Princeton) for lending us the microwave sweeper and quadrupler (described in section 1.3) that made the work presented in chapter 3 possible. Thank also to Warren S. Warren for lending us the HP 8350B/83595A microwave source, and Brooks H. Pate (congratulations for the MacArthur) for the active doubler/amplifier used in the low frequency experiment presented in section 3.3.2. Dorine, don’t you worry ... I won’t borrow anything from you anymore.

Special thanks to a very special bunch of people: Thomas Esser and Gerben Wierda (teTeX), Richard Koch, Jérôme Laurens, Dirk Olmes and Gerben Wierda (TeXShop), Han The Thanh, Petr Sojka, and Jiri Zlatuska (pdfL<sup>A</sup>TeX), Vincent Darley (BibTeX), Rick Zaccone (MakeIndex), Rick Zaccone and Robert Gottshall (Excalibur), Thomas Williams, Colin Kelley and many others (Gnuplot).

And let's not forget everybody at some big, Big, BIG, BIG corporation in Redmond, WA, for continuously developing (and of course *improving*) their fine family of operating systems, thus convincing me that Apple Computer just does everything better.

Oh, I almost forgot ... Let's thank Al Gore for inventing The Internet. It makes everything so much simpler: communicating *via* email, ordering goodies, and especially writing a thesis from the other end of the country.

### **The Butler Trailer Park**

Peter "Big K" Khalifah ... what will I do with all those bike parts, now that your rolling wreck is about 2000 miles from my toolbox? Scott, I had never seen so much climbing gear spread over someone's bed. Where were you sleeping? Richmond, I had such a great time sharing the 300C with you, I had to follow you to Pasadena. Adriana, Paul, the people from The Old World. I hope that your little introduction to the life in the New World was a pleasant experience.

Lester (the big yellow cat) and Blanca (the cute little white cat) ... it was nice to have you guys around. I hope your people didn't mind too much that I was feeding you all the time. Did you tell them I was buying better food? MMMmmmm, lamb and rice!

## Personal . . .

Henry, the Big Guy, the sweetest puppy around (sometimes known as 95 pounds of grumpy brown dog). Thanks for hanging out with me, every single day I stayed at home to write this thesis. Now you're gone. You have no idea how much I miss you. If you see my dad, tell him I miss him too . . .

Tinker Bell (Tinky, . . . Stinky when you're not nice). Life with you is like being continuously surrounded by this strange, noisy, white blur. I promise I'll always try to run faster. Someday, you won't be pulling anymore!

Maman. Merci pour tout. Ca doit être pénible de toujours attendre mes visites, et de me voir repartir quelques misérables petits jours plus tard. Désolé. J'espère que tu vas venir le visiter, ton petit André. C'est à ton tour de voyager maintenant. On a une chambre de libre, juste pour toi . . .

Doris and Pat, a.k.a. "Maggie's Parents", thanks for the apartment, for all those Dinner and Bridge evenings, the Magic Castle, the bees, everything.

Meg, thanks for being my sweetheart. It just can't be easy to live with such a pouty boy. Our life in Princeton wasn't easy. Then, you moved to Maine. Stunning phone bills, 8–9 hours drive at night: it wasn't easy. Now that we live together, life will get easier. You'll see . . .

I love you.

For all the forgotten ones: Thanks . . . you know who you are!

This thesis has been written, and cursed at, on a PowerBook running Mac OS X.

This is the room of the wolfmother wallpaper. The toadstool motel you once thought a mere folk tale, a corny, obsolete, rural invention.

This is the room where your wisest ancestor was born, be you Christian, Arab, or Jew. The linoleum underfoot is sacred linoleum. Please remove your shoes. Quite recently, the linoleum here was restored to its original luster with the aid of a wax made from hornet wax. It scuffs easily. So never mind if there are holes in your socks.

This is the room where your music was invented. Notice the cracked drumhead spiked to the wall, spiked to the wolfmother wallpaper above the corner sink where the wayward wife washed out her silk underpants, inspecting them in the blue seepage from the No Vacancy neon that flickered suspiciously out in the thin lizard dawn.

What room is this? This is the room where the antler carved the pumpkin. This is the room where the gutter pipes drank the moonlight. This is the room where moss gradually silenced the treasure, rubies being the last to go. Transmissions from insect antennae were monitored in this room. It's amazing how often their broadcast referred to the stars.

A clue: this is the room where the Painted Stick was buried, where the Conch Shell lay wrapped in its adoring papyrus. Lovers, like serpents, shed their old skin in this clay room. *Now* do you remember the wallpaper? The language of the wallpaper? The wolfmother's blood roses that vibrated there?

Enough of this wild fox barking. You pulled up in the forest Cadillac, the vehicle you claimed you'd forgotten how to drive. You parked between the swimming pool and the row of blackened skulls. *Of course*, you know what room this is.

This is the room where Jezebel frescoed her eyelids with history's tragic glitter, where Delilah practiced for her beautician's license, the room in which Salome dropped the seventh veil while dancing the dance of ultimate congition, skinny legs and all.

*Tom Robbins, 1990*

# Contents

<b>Abstract</b>	<b>iii</b>
<b>Acknowledgements</b>	<b>v</b>
<b>Contents</b>	<b>x</b>
<b>Figures</b>	<b>xiii</b>
<b>Tables</b>	<b>xv</b>
<b>Introduction</b>	<b>1</b>
Historical Perspective . . . . .	2
Helium Nanodroplet Isolation Spectroscopy . . . . .	6
Theoretical Advances . . . . .	7
HENDI as a Tool for Synthesis . . . . .	10
Outline of the Dissertation . . . . .	12
<b>1 Experimental Methods</b>	<b>14</b>
1.1 Molecular Beam Hardware . . . . .	14

1.1.1	General Characteristics of HENDI Spectrometers . . . . .	14
1.1.2	Big Sur . . . . .	16
1.1.3	Cloud II $\mathcal{E}$ . . . . .	27
1.2	Ultraviolet/Visible Spectroscopy . . . . .	29
1.2.1	Introduction . . . . .	29
1.2.2	The Evolution X/Indigo Laser System . . . . .	30
1.2.3	Multi-Pass Cell and Beam Depletion . . . . .	32
1.2.4	Fluorescence Collection . . . . .	35
1.3	Microwave Spectroscopy . . . . .	39
1.3.1	Introduction . . . . .	39
1.3.2	Sweeper and Multiplier Head . . . . .	40
1.3.3	Waveguide and Detection of Beam Depletion . . . . .	40
<b>2</b>	<b>Photolysis of NO<sub>2</sub>: Formation of Radicals <i>In Situ</i></b>	<b>43</b>
2.1	Introduction . . . . .	44
2.2	Electronic Excitations of NO <sub>2</sub> . . . . .	47
2.3	Droplet Beam Depletion Experiment with NO <sub>2</sub> . . . . .	51
2.3.1	Calibration of the Pickup Cell . . . . .	51
2.3.2	Beam Depletion of NO <sub>2</sub> . . . . .	51
2.4	LIF of NO <sub>2</sub> . . . . .	54
2.5	Relaxation Mechanism . . . . .	58
2.6	Outlook: LIF of NO . . . . .	61

2.6.1	Two-Photon $A - X$ Transition . . . . .	62
2.6.2	One-Photon $A - X$ Transition . . . . .	65
<b>3</b>	<b>Breakdown of the Adiabatic Following Approximation</b>	<b>66</b>
3.1	Introduction . . . . .	67
3.2	Microwave Spectroscopy of HCN and DCN . . . . .	71
3.3	Microwave Spectroscopy of CH <sub>3</sub> F and CD <sub>3</sub> F . . . . .	78
3.3.1	The Spectroscopy of Symmetric Tops . . . . .	78
3.3.2	Microwave Spectra of CH <sub>3</sub> F and CD <sub>3</sub> F . . . . .	80
	<b>Conclusions</b>	<b>87</b>
	<b>Bibliography</b>	<b>90</b>

# List of Figures

1.1	Diagram of Big Sur . . . . .	17
1.2	Diagram of the JEFF Preamplifier . . . . .	20
1.3	Schematics of the Nozzle . . . . .	21
1.4	Temperature Dependence of the Beam Signal . . . . .	25
1.5	High Temperature Oven . . . . .	26
1.6	Diagram of Cloud II $\epsilon$ . . . . .	28
1.7	Schematics of the Indigo Cavity . . . . .	32
1.8	Layout of the Indigo's Internal Components . . . . .	33
1.9	Multipass Cell Design . . . . .	34
1.10	Multipass Laser Beam Path . . . . .	35
1.11	Fluorescence Collector . . . . .	36
1.12	Lens Mount Assembly for LIF Collector . . . . .	38
1.13	Microwave Cell . . . . .	41
2.1	Potential Energy Surfaces of NO <sub>2</sub> , and Dissociation Process . . . . .	50
2.2	Pickup Effects on Beam Signal . . . . .	52

2.3	Pickup Pressure Dependence of NO <sub>2</sub> Signal . . . . .	53
2.4	NO <sub>2</sub> Beam Depletion Spectrum . . . . .	55
2.5	Gas Phase Fluorescence Spectrum of NO <sub>2</sub> . . . . .	56
3.1	Rotational Spectra of HCN and DCN . . . . .	72
3.2	Saturation Behavior of HCN and DCN . . . . .	73
3.3	HCN spectrum with best fit . . . . .	75
3.4	DCN spectrum with best fit . . . . .	76
3.5	Rotational Spectrum of CH <sub>3</sub> F . . . . .	81
3.6	Rotational Spectrum of CD <sub>3</sub> F . . . . .	82

# List of Tables

3.1	Best Fit Parameters from the Saturation Data of HCN and DCN . . .	74
3.2	Moments of Inertia of HCN and DCN . . . . .	77
3.3	Moments of Inertia of CH <sub>3</sub> F and CD <sub>3</sub> F . . . . .	83

# Introduction

The work described in this dissertation focuses on the experimental development of a technique called HELium NanoDroplets Isolation (HENDI) spectroscopy [1, 2]. HENDI is a form of matrix isolation where the host, a beam of helium droplets of  $10^3$  to  $10^4$  atoms, is formed by adiabatic expansion of helium from a cold nozzle into vacuum. Doping of these droplets proceeds *via* a pickup process as the beam travels through a scattering cell containing a low pressure (on the order of  $10^{-4}$  Torr) of the species of interest. After pickup, most of the droplets can be considered a nanoscopic “test-tube” containing the dopant of choice, solvated in a small quantity of liquid helium. As the droplets cool down evaporatively to 0.38 K, they become superfluid and allow *rotationally resolved* high-resolution spectroscopy to be performed on very cold guest molecules. Recently, the scientific community’s appreciation of the method has been furthered by theoretical advances that allow the precise prediction of both the location of the guest species [3] (whether they are fully solvated, or adsorbed on the surface) and the change of their moment of inertia [4–6] as the molecule moves from the gas phase to its solvated location.

HENDI offers an elegant alternative to conventional matrix isolation spectroscopy techniques that were first developed almost 50 years ago [7]. Traditionally, small amounts (say, less than 1%) of the species of interest are codeposited with

some inert substance (usually a rare gas, like neon or argon) on a cold, transparent surface where absorption or fluorescence spectra can be measured. As the low temperature of the matrix hinders the mobility of the guests, thus preventing reaction, recombination, or other unwanted guest–guest interactions, the measurements can be performed over extended periods of time. Using photons of high enough energy even from weak sources, it is in this way also possible to photolyze photolabile species and characterize the photolysis products *in situ*. This chapter will describe the evolution of the field of matrix isolation, towards the development of HENDI, before closing in giving an outline of the dissertation.

## Historical Perspective

The first mention of the idea of isolating molecules in a matrix in order to observe gas–like properties from “condensed” species appeared in a 1924 paper, *The Light Emitted From Solidified Gases and its Relation to Cosmic Phenomena*. Prof. L. Vegard, whose research on solid nitrogen was focused on the understanding of the role of nitrogen emission in the auroral spectrum, proposed the following:

“When an inert gas which contains traces of nitrogen is condensed on the cold surface, the layer will contain small nitrogen particles surrounded by an inert substance. In this state, we should expect nitrogen to behave in a similar way as if the particles existed in free space.” [8]

This insightful comment turned out to be exactly what motivated Whittle, Dows and Pimentel when, in 1954, they published *Matrix Isolation Method for the Experimental Study of Unstable Species* (thus coining the term “matrix isolation”).

Their main interest was aimed at the development of a new method of studying free radicals and unstable substances, and the experimental advance they proposed was described as follow:

“The matrix isolation method proposed here involves accumulation of a reactive substance under environmental conditions which prevent reaction. The intent of the method is to trap active molecules in a solid matrix of inert material, crystalline or glassy. If the temperature is sufficiently low, the matrix will inhibit diffusion of the trapped molecule, thus holding the active molecules effectively immobile in a nonreactive environment.” [7]

They achieved their goal, as they observed that different matrices do indeed prevent reactions from occurring: for example, the spectrum of 1%  $\text{HN}_3$  in a matrix of  $\text{CCl}_4$  *did not* show evidence for the presence of hydrogen bonded species, thus demonstrating the ability of the matrix of isolating individual dopants from each others.

Later, matrix isolation studies by Milligan and Jacox did show that the cold, inert environment created by solid rare gases could be used to interrogate exotic species. They first suggested that if atoms could diffuse through rare-gases matrices, it would be possible to generate, and stabilize free-radicals made by atom-molecule reactions in the matrix. Following the photolysis of HI (into H and I radicals) in an  $\text{O}_2$ -doped argon matrix [9], they observed the formation of the radical  $\text{HO}_2$ . Then, they proposed that the matrix could stabilize the photodissociation products of a precursor molecule into fragments when there is a significant barrier to recombination. They attempted the photolysis of methyl azide ( $\text{H}_3\text{CNNN}$ ), in

argon and nitrogen, and they observed the formation of the products  $N_2$  and  $H_3CN$  (a diradical). Unfortunately,  $H_3CN$  very rapidly rearranges into  $H_2CNH$ , a stable, closed-shell molecule. However, they noticed that upon further irradiation, the major decomposition product of  $H_2CNH$  was found to be  $HNC$ , an isomer of  $HCN$ , the existence of which had been proposed on the basis of theoretical predictions, but had never been observed [10].

Despite some obvious drawbacks, mainly the absence of rotational resolution, and the occurrence of relatively large vibrational shifts (features globally referred to as “matrix effects”), matrix isolation spectroscopy became a very successful technique for the study of unstable molecular species. The rapid evolution of laser technology, since its first development in the early 60’s, has provided experimentalists with a new and highly efficient means of interrogating and analyzing their samples. Novel deposition techniques, like laser vaporization, also benefited from the increasing availability of lasers, and by the mid 80’s, scientists were routinely studying matrix isolated transients (reactive intermediates) involving metals, alloys, and clusters of all sorts. Even after the introduction of supersonic jet spectroscopy, which provides the advantages of gas phase spectroscopy in a cold (down to a few Kelvins) and quasi-collisionless environment, matrix isolation has proved to be the method of choice for the study of weak, or even forbidden, transitions. In many instances, the presence of the matrix relaxes the selection rules, thus permitting the study of previously unreachable electronic states. The environment may also allow non-radiative relaxation from “allowed” states to states of different symmetry and spin state, which can then be studied spectroscopically.

As the deposition process allows the accumulation of reasonably large quantities of the species of interest, over several minutes or even hours, even not-too-

sensitive characterization techniques, such as absorption spectroscopy, can be used, thus permitting the *survey* of spectral features of novel molecules, ions or radicals. Such data can then be used to direct, and facilitate, a thorough interrogation by means of a more sensitive technique like laser induced fluorescence (LIF), or even form the starting point for a high resolution molecular beam study. In recent years, the field of matrix isolation spectroscopy has gotten even more popular with the introduction of quantum matrices. Experiments performed in isotopes of hydrogen (*ortho* and *para* H<sub>2</sub>, HD, and D<sub>2</sub>) have shown important quantum effects, as the zero-point motion of the constituents of the matrix is a good fraction of the distance between nearest neighbors. Also, because hydrogen molecules composing the matrix are known to be able to rotate in the solid and because all the isotopes have such different vibrational and rotational properties, great details about the (nonradiative) relaxation of guests embedded in such matrices can be obtained. Consequently, matrix effects initially viewed as undesirable, became the focus of the experiment. In parallel with the development of hydrogen matrices, spectroscopy performed in liquid helium is offering new possibilities. Both isotopes, <sup>3</sup>He and <sup>4</sup>He, have liquid phases, with <sup>4</sup>He-II being *superfluid* below  $T_{\lambda}=2.174$  K. Although <sup>4</sup>He cannot be solidified under ambient pressure, studies of doped solid helium have been performed in high-pressure cells, which could be compared to previous experiments performed in traditional rare-gas matrices (Ne, Ar, Kr, and Xe). The study of impurities solvated in bulk liquid (superfluid) helium is not easily achieved because of difficulties in seeding the matrix in a controlled manner. Laser vaporization of targets directly immersed in the liquid facilitates doping, but since most helium/impurity pair potentials show weaker interactions than impurity/impurity potentials, aggregation of dopants is unavoidable. Furthermore, many dopants also exhibit favorable interactions with the containing vessel walls, where they tend to adsorb, and no longer

belong to the “bulk”. For impurities that feature unfavorable interactions with helium, another difficulty inherent to their introduction into bulk helium arises: the existence of a large barrier to solvation (the repulsive potential at the liquid surface) prevents immersion.

An elegant way to circumvent the problem of impurity aggregation/exclusion was devised in the early 90’s, as the idea of seeding *one*, small, “droplet” of helium with *one* impurity was introduced. The sticking of molecules to a beam of argon clusters (the “pickup” technique) had been studied by Scoles and coworkers for a number of years [11, 12], and the idea of embedding impurities into helium droplets appeared to effectively eliminate both aggregation (as only one dopant was present in each droplet) and dopant “wall” segregation (as no container was needed in this case). It soon became clear that HENDI spectroscopy would combine the advantages of beam spectroscopy, *and* those of matrix isolation techniques.

## Helium Nanodroplet Isolation Spectroscopy

Since the early HENDI experiments performed by the group of Toennies on the pickup of impurities by a beam of helium droplets [13], and the first spectroscopic interrogation of impurities ( $\text{SF}_6$ , and  $(\text{SF}_6)_2$ ) embedded in helium droplets by the group of Scoles [1, 2], the field has continuously gained in popularity. Especially noteworthy are the experiments of Hartmann *et al.* [14], where results obtained with a series of line-tuneable  $\text{CO}_2$  lasers [2] were reinvestigated using a high-resolution, continuously tuneable diode laser. The rotational structure of the infrared spectra of the monomer was resolved, and the temperature of the droplets was experimentally determined to be 0.38 K, a value that is near the theoretical estimate

of 0.32 K [15, 16]. A few years later, another landmark experiment performed by the group of Toennies demonstrated the superfluid character of the droplets, when they are larger than some critical size of approximately 60 atoms [17], again corroborating earlier theoretical predictions [18] concerning the size requirements for the onset of superfluidity. This fascinating near-lack of viscosity in helium nanodroplets, along with the ability to cool, and maintain, embedded guests to a temperature of 0.38 K, has made HENDI the method of choice for the study of solvation effects in *simple* solvents. As superfluid helium represents the least perturbative solvent one can imagine, the spectra of impurities solvated in helium has shown striking resemblances with spectra measured in the gas phase: linewidths as narrow as 80 MHz (in the microwaves [19]) and 675 MHz (for *overtone*s in the infrared [20]) have been observed by our group. By comparison, resonances observed in solid matrices are considered *very sharp* when narrower than  $\sim 2 \text{ cm}^{-1}$  (60 GHz). Furthermore, the infrared spectra feature small shifts of vibrational band origins (on the order of a few  $\text{cm}^{-1}$ ) while the symmetry of the guest is conserved, despite a sometimes pronounced slow down of the rotation. The latter is proportional to the non-sphericity of the rotating molecule and is due to the inertia of the helium atoms moving in synchronism with the rotor. The resulting increase in the effective moment of inertia causes the rotational structure to “contract”.

## Theoretical Advances: Hydrodynamic Model

Recent efforts in our group yielded the formulation of a model that allows for the explanation of the observed increase of the moment of inertia of rotors embedded in superfluid helium. The details of this model have already been published [4, 6], and only an introduction will be given here: a detailed discussion can be found in Carlo

Callegari’s thesis [21]. The model is based on the notion that the rotation of a rigid body in superfluid helium produces fluid displacement, which leads to an increased inertia. Such a hydrodynamic contribution to the effective moment of inertia of a molecule solvated in an ideal liquid of uniform density (equal to that of bulk liquid He) had been considered earlier but had been found to be a small fraction of the experimental value [4, 17, 22]. Hydrodynamic calculations that properly account for the increased He density around the solute molecule and its anisotropy [6] have been performed: The calculated increase in the rotational inertia was found to be in semi-quantitative agreement with the observed effective moments of inertia measured for several molecules [6, 21]. An important assumption of the hydrodynamic model is that while the helium flow remains irrotational, the fluid’s *density* adiabatically follows the rotation of the molecule, much like a wave.

Fixed-frame Diffusion Monte Carlo (DMC) calculations for SF<sub>6</sub> have found, however, that the helium density does not perfectly follow the molecular rotation [5]. When the static rotational constant of the free SF<sub>6</sub> molecule was artificially increased by a factor of 10, greatly increasing the rotational speed, the modulation of the helium density in the rotating molecular frame as well as the corresponding solvation-induced increase in the moment of inertia were substantially reduced. Experiments have found that fast rotors display a smaller variation of their rotational constant than slower rotors do, which seems to corroborate the behavior predicted by what we called the “breakdown of the adiabatic following approximation” (when the angular velocity of the rotor increases beyond some value, the superfluid can no longer follow the rotational motion, and the adiabatic following breaks down). Unfortunately, a comparison of rotational speed alone cannot account for the observed change in moment of inertia, because the molecules studied differ widely in shape: the faster rotors, because of their (usually) simpler structure, exhibit a more

isotropic interaction potential than the slower ones, that tend to be more complex molecules. In order to study the emergence of the adiabatic following, one must devise an experiment that allows to fine-tune the rotational velocity of a rotor, *without* modifying the interaction potential with helium. Isotopic substitution can achieve such goal. Because different isotopes only differ by the number of neutrons in their nucleus (only the mass of the atoms differ), their electronic properties are nearly identical. Consequently, one may consider that the pair potential between helium and an impurity will not be affected by isotopic substitution in the impurity, except for small corrections due to changes in zero-point averaged structure. For that reason, an experiment aimed at observing the pure rotational spectra of isotopic pairs of molecules has been performed, and will be described in Chap. 3 of this dissertation. The spectra of HCN and CH<sub>3</sub>F will be compared to those of DCN, and CD<sub>3</sub>F, observing for the first time, the breakdown of the adiabatic following approximation.

As our understanding of the droplet-induced matrix effects improves, the development of experimental techniques taking full advantage of the amazing properties of superfluid helium must be pursued. Important results from traditional matrix studies could be repeated and improved upon with HENDI, if rotational information could be obtained, and *understood*. Furthermore, because of the weakness of the interaction between the guest and the droplet, and its much lower temperature, HENDI allows for experiments that cannot be carried out using solid state matrix isolation. The following section will introduce HENDI as the ideal synthetic tool for cryochemistry.

## HENDI as a Tool for Synthesis

Apart from the ability to rotationally resolve the spectra of embedded species, HENDI provides spectroscopists with an easy and efficient way to cool molecules. Experiments have shown that the cooling rate upon solvation in helium is tremendous: after pickup, the dopant's energy is released into the droplet which then evaporatively cools back down to 0.38 K, each evaporated helium atom dissipating between 5.5 and 7 K [23]. When more than one pickup occurs, the guests are free to explore the whole volume of the droplet, and meet. In most cases, chemical reactivity will be hindered by the heat bath being unable to supply more energy than  $kT$  (3 J/mol, or  $8 \times 10^{-4}$  kcal/mol at 0.38 K). As expected, unimolecular processes are slowed down as well, which makes possible the observation of unstable species for at least the duration of an experiment (limited by the time-of-flight, about a millisecond in our case). The observation of trimers of Na atoms in the unusual high-spin quartet state demonstrated the unparalleled possibilities of HENDI [24] at stabilizing exotic species. As three sodium atoms meet on the surface of the droplet, all their spins are parallel, and the low temperature of the bath prevents them from rearranging into a lower energy electronic configuration: a van der Waals trimer is formed, in the *quartet* state.

Work by Nauta and Miller on the formation of oligomers of both HCN and HCCCN [25, 26] showed that the aggregation of monomers into van der Waals complexes does not follow the same rules that are valid in the gas phase. Only linear complexes of these molecules have been observed in helium. In helium, rapid cooling forces each additional unit to adopt a (locally) low energy configuration at each step of the aggregation process: once a complex is partially formed, the addition of another unit does not allow the reorganization of the whole structure. The

aggregation process is guided by long-range forces (dipole-dipole interactions) that steer the molecules into adopting a linear, hydrogen-bonded configuration. The maximum size of these oligomers obeys a strict rule, as the length of the chain is limited by the diameter of the droplet. More recent experiments by Nauta and Miller have focused on aggregates of water [27]. The conclusions of their work are that, up to the pentamer,  $(\text{H}_2\text{O})_5$ , the structure formed in helium nanodroplets is identical to the corresponding one formed *via* supersonic expansion in a slit jet [28]. However, the hexamer behaves otherwise: The structure observed in helium is cyclic and hexagonal, like the one found in common ice. In the gas phase, the hexamer adopts a cage-like structure that appears to be the global energy minimum of such isolated complex. The different behavior induced by the two environments can be rationalized as follows. In the gas phase, there is no barrier to reorganization as the complex is formed and the true energy minimum can be reached. Furthermore, small energy barriers affecting conformational changes can be easily overcome by the energy released upon complexation. In helium nanodroplets, as the molecules are rapidly cooled by the helium bath as the complex is formed, no energy is available to push the structure out of local energy minima. Also, there is a large energy penalty associated with out of plane motion as the cyclic oligomer is assembled up to the pentamer, and only a hexagonal hexamer can form upon addition of another unit. Unlike the cases of both HCN and HCCCN, where only linear species are observed, water forms bent polymers as the monomer itself is not a linear molecule. The unfavorable energetics associated with further bending of the complex to “close the cycle” are compensated for by the energy released by the formation of another hydrogen bond. These results demonstrate the high selectivity of the complexation processes in helium nanodroplets, where long range interactions dominate the preliminary steps of oligomer formation, and the low temperature forbids further re-

arrangement towards global energy minima. They emphasize the idea that a beam of nanodroplets can be viewed as a beam of “test-tubes”, where exotic complexes may be formed, stabilized, and interrogated.

## Outline of the Dissertation

The body of this dissertation consists in three chapters. Chapter 1 will present the experimental details of the apparatus. Section 1.1 will outline the fundamentals of nanodroplet formation, and analyze the features of the different spectrometers used to collect the data. Section 1.2 focuses on the laser system used to generate ultraviolet radiation needed for the photolysis experiment. Finally, the microwave system used to record the spectroscopic evidence for the breakdown of the adiabatic approximation will be described in section 1.3.

In chapter 2, a brief survey of the chemistry and spectroscopy of  $\text{NO}_2$  and its dissociation products  $\text{NO}$  and  $\text{O}$  will be presented. Then, beam depletion data recorded from 400 to 368 nm will show that  $\text{NO}_2$  *does not* dissociate, even at energies exceeding the gas phase threshold ( $25\,128.57\text{ cm}^{-1}$ ) by about  $2000\text{ cm}^{-1}$ . The absence of fluorescence emitted from the embedded species (it has been observed only from gas phase  $\text{NO}_2$ ) confirms that vibrational relaxation is much faster than dissociation. The actual relaxation pathway is not known at present, as it is not clear whether or not the dissociation products form and immediately recombine, or simply don't appear at all. An experiment aimed at probing  $\text{NO}$  during the relaxation process has been designed, and the details are presented.

Then, in chapter 3, pure rotational spectra of isotopically substituted

species will be presented. The resonances observed at 72.27 and 59.9 GHz (for HCN and DCN, respectively) are assigned to the  $J=0 \rightarrow 1$  transition. These values enable the calculation of the *effective* moment of inertia, and a comparison to the gas phase moments of inertia: The slowest rotor (DCN) displays a larger increase by about 10%. This observation provides evidence for the breakdown of the adiabatic following approximation. For  $\text{CH}_3\text{F}$  and  $\text{CD}_3\text{F}$ , the analysis is not as simple, as the observed resonances (43.2 and 36.1 GHz, for  $\text{CH}_3\text{F}$  and  $\text{CD}_3\text{F}$ , respectively) cannot be assigned. Our failure to observe microwave signal at half the observed transitions is not conclusive because of poor signal-to-noise ratio. Consequently, the observed transitions could be the  $J=0 \rightarrow 1$ , as well as the  $J=1 \rightarrow 2$ . The effect of the displacement of the center of mass (upon isotopic substitution) on the “dynamical sphericity” has been simulated. These results show that the observed transition is likely to be the  $J=0 \rightarrow 1$ . A short conclusion section will close the dissertation.

# Chapter 1

## Experimental Methods

### 1.1 Molecular Beam Hardware

The experiments described in this dissertation have been performed on two distinct HENDI spectrometers, using a variety of radiation sources. The ultraviolet/visible experiments were carried out with the Big Sur spectrometer, whereas the microwave experiments were carried out with the Cloud II $\epsilon$  machine. An outline of the nanodroplets beam preparation, followed by a brief description of both apparatus will be given.

#### 1.1.1 General Characteristics of HENDI Spectrometers

A beam of helium droplets is produced by supersonic expansion of high pressure He gas (99.9999 % purity) from a cooled nozzle, into a vacuum chamber. In the

very early stages of the expansion, condensation of the cooled helium gas into nanodroplets is triggered by many-body collisions: two-body collisions are inefficient at condensing the gas, at least a third body is needed to release the excess energy. The average droplet size  $\langle N \rangle$  is controlled by setting the nozzle temperature, at constant backing pressure (for the experiment presented in this dissertation, in the range 15–35 K, actively stabilized within 0.1 K [29]) and is estimated by means of known scaling laws with the following equation [30, 31]

$$\langle N \rangle \propto \frac{p d^{1.5}}{T^{2.4}} \quad (1.1)$$

from the backing pressure  $p$ , the nozzle diameter  $d$  and the expansion temperature  $T$ . Experimental determination of the size of helium droplets has been published by Lewerenz *et al.* [32]. At an expansion temperature of 16 K, for a 5  $\mu\text{m}$  nozzle under 80 bar of pressure, they found  $\langle N \rangle = 7\,220$ . Only values for  $T = 24$  K ( $\langle N \rangle = 3\,170$ ), and  $T = 14$  K ( $\langle N \rangle = 14\,400$ ) were also reported in Ref. 32. These values, along with equation 1.1 can be used to generate the following equation

$$\langle N \rangle = 0.542 p d^{1.5} \quad (1.2)$$

where the temperature is taken to be 16 K (the limiting value for our setup, see section 1.1.2) and the pressures have been converted to psi (for convenience). The nozzle diameter is expressed in  $\mu\text{m}$ . When using equation 1.2 for a 10  $\mu\text{m}$  nozzle, and 800 psi of helium backing pressure, one gets an average droplet size of about 13 700 atoms. In this work, the value 14 000 will be reported as the large droplet limit.

About 10 mm downstream of the expansion, the center portion of the beam is admitted into a second vacuum chamber, through a skimmer, where it passes

through a small cell containing the analyte (gas) of interest, which is captured very efficiently by the droplets. The pressure in the cell (typically  $10^{-4}$  torr  $\approx 10^{-2}$  Pa, for a 25 mm long cell) is adjusted to maximize the amount of singly-doped droplets, which can be monitored spectroscopically. After pickup, fast relaxation of all the degrees of freedom of the guest occurs, the energy being released by evaporation of helium atoms (about 500 for the pickup of a typical molecule at room temperature). Each and every seeded nanodroplet can then be seen as a nanoscopic test-tube, isolated from the others in a collisionless environment, flying at about 450 m/s in a specific direction. Spectroscopic interrogation is achieved by letting the doped droplets cross one or more radiation fields (two in the case of double resonance experiments [33, 34]) and the absorption of a photon is monitored either by collecting laser-induced fluorescence or measuring the droplet beam depletion (caused by the relaxation-induced helium evaporation) by means of a bolometer detector located on the beam path downstream of the laser-crossing point.

### 1.1.2 Big Sur

This spectrometer has gone through several important modifications since the last series of experiments were performed (see references 3, 35, 36): A new detector has been added, the helium droplet source (nozzle and skimmer) has been completely refurbished, and a metal furnace has been modified and added to be used as a pickup cell. A complete account of all these changes will be given in the following subsections. First, a description of the machine is provided. As seen in figure 1.1, the helium expansion occurs in the middle chamber; the large vacuum chamber on the left is an interface between the machine and the large 32 000 l/s diffusion pump. After the expansion, the helium beam transfers to the detection chamber, *via* a 380  $\mu\text{m}$

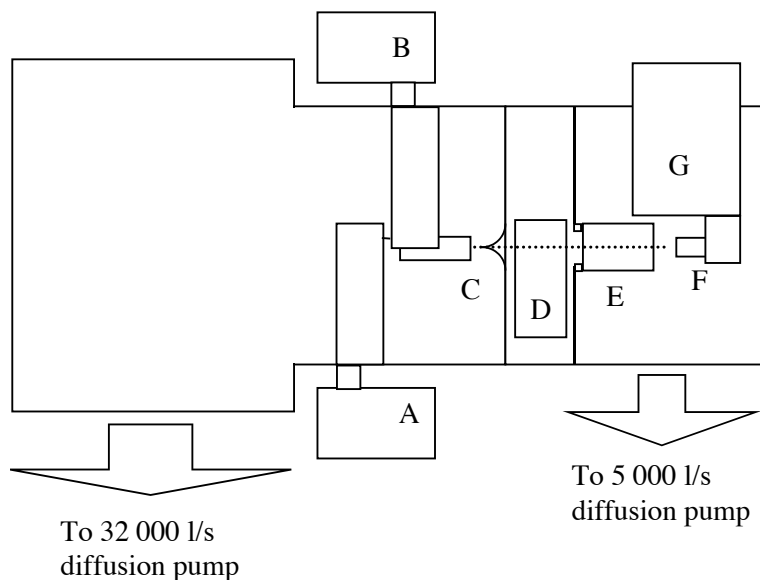


Figure 1.1: Diagram of Big Sur. A: pre-cooler for the gas line, B: cooler for the nozzle, C: nozzle (facing the skimmer), D: side view of the oven/pickup cell, E: location of either the multipass cell, or the fluorescence collector, and finally the bolometer F: with its liquid helium cryostat G. The 32 000 l/s diffusion pump pumps on both the left chamber and the expansion chamber, up to the skimmer. The 5 000 l/s only pumps the small detection chamber, containing items D, E, F, and G.

skimmer [37]. About 10 mm from the skimmer, the droplet beam passes through the oven/pickup cell where it is doped with the impurity of interest. Immediately after doping, the droplets either cross the laser beam orthogonally in the fluorescence collector, or interact with multiple crossings of the laser in the multi-pass cell. Fluorescence is collected immediately in the interaction zone, whereas beam depletion is observed on a liquid helium cooled bolometer, some 50 mm downstream.

## The Thermal Detector

A surface ionization detector that had been used for many successful alkali beam depletion experiments has been replaced by a bolometer suitable for both helium, and hydrogen droplet experiments [38]. Unlike standard bolometers that are optimized to operate at the lowest possible temperature, this bolometer has been designed to operate at a temperature *higher* than the boiling point of helium. The higher operating temperature (about 5–6 K, according to the manufacturer) facilitates the desorption of hydrogen molecules which condense on the surface of the detector upon impact (the desorption rate varies exponentially with temperature below the freezing point of hydrogen, 13 K), as a layer of frozen hydrogen would lower the sensitivity and affect the frequency response of the device.

The bolometer features a thin layer of nichrome, plated to the back of the absorber. It acts as a heater resistor (of about 600  $\Omega$ , see Fig. 1.2) which allows the operating temperature to be kept rather high, even if the helium bath in the cryostat is around 1.6 K, below the  $\lambda$  transition (2.1 K), to reduce microphonic noise due to boiling (as a superfluid evaporates exclusively from its own surface). The optimal heating rate (thus the operating temperature) is found by varying the current to the heater by means of an external variable resistor (see Fig. 1.2). When the correct value is found, *i.e.* when the resistor is set such that the bolometer signal is maximized, the trimming circuit has to be replaced by a fixed resistor of the same value in order to reduce contact noise intrinsic to all variable resistors.

For the helium droplet experiment, this “hotter” bolometer is inferior to the standard “cold” bolometer that is installed in the Cloud II $\epsilon$  apparatus (see Section 1.1.3), as both the sensitivity and the noise equivalent power are affected by the

modification and, globally, a factor of three is lost in signal-to-noise. Nevertheless, this slight disadvantage is, in our case, fully compensated for by the larger effective solid angle of this machine (owing to its shorter beam path and the round, 3 mm aperture of the bolometer mask) such that Big Sur offers better overall performance than Cloud II $\mathcal{E}$ .

When Cloud II $\mathcal{E}$  was transformed into a helium droplet machine (see Carlo Callegari’s thesis, Ref. [21]), it was observed that vibrations from the compressors and the cold heads were generating a large amount of microphonic noise at the bolometer, mostly due to by pickup from the long small-gauge wires. Fortunately, this kind of noise has a very simple cure: lowering the output impedance of the detector. To achieve this, Infrared Laboratories manufactures and sells a JFET preamplifier package [39] that mounts directly to the cold finger that supports the bolometer. Instead of driving long wires outside the machine, and into the lock-in amplifier’s preamplifier, the bolometer is *directly* attached to the gate of the JFET (see Fig. 1.2). It reduces the impedance of the bolometer by 5 orders of magnitude, from about 12 M $\Omega$  to 500  $\Omega$  [40]. The amplifier has to be kept at an operating temperature of about 70 K, which is insured by a resistive heater (the 61 k $\Omega$  resistor on Fig. 1.2) directly attached to the thermally insulating mount, next to the transistor. Careful design of the mount insures that the heater does not provide much heat to the bolometer, and the presence of the preamplifier doesn’t appreciably affect the boiloff rate of the helium in the cryostat.

## Determination of the Nozzle Diameter

An important step in the characterization of the source is to get an experimental value for the nozzle diameter. According to the manufacturer [43], it is nominally

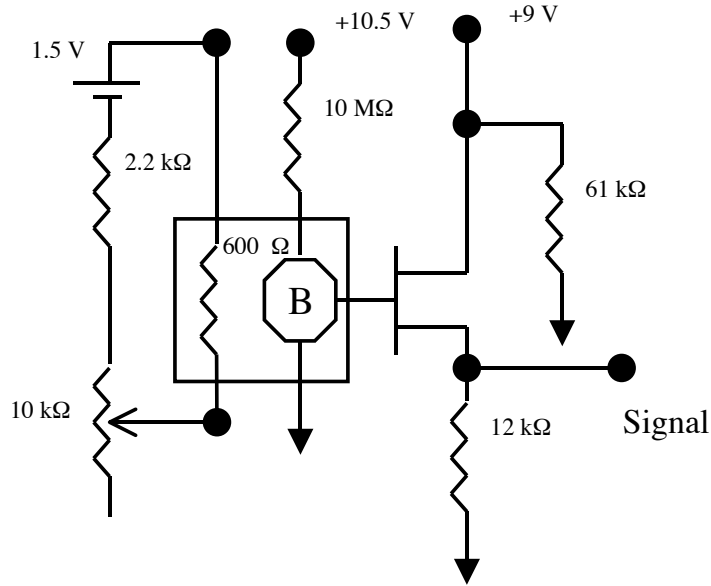


Figure 1.2: Diagram of the electrical connections of the bolometer and JFET preamplifier. The circuit that connects to the heater (represented by a the  $600\ \Omega$  resistor) is floating to minimize current noise. The Signal connector is read by the lock-in amplifier [41] *via* a voltage preamplifier [42]. The  $61\ \text{k}\Omega$  resistor acts as a heater for the JFET.

$10\ \mu\text{m}$ , but variations in the manufacturing process lead to size irregularities which may, to a certain extent, affect the performance of the source. The nozzles manufactured at the Princeton University Chemistry Machine Shop, are cylindrical. A platinum microscope aperture ( $3.04 \times 0.25\ \text{mm}$ ) is forced inside a tiny groove at the tip of the nozzle (see Fig. 1.3 B<sub>1</sub>) and held in place by rolling the tip such that physical deformation of the material (in our case copper, for optimal thermal conduction) clamps the disc against the wall of the tube, as shown on Fig. 1.3 B<sub>2</sub>. Note that both the deformation and the size of the aperture are grossly exaggerated on the diagram.

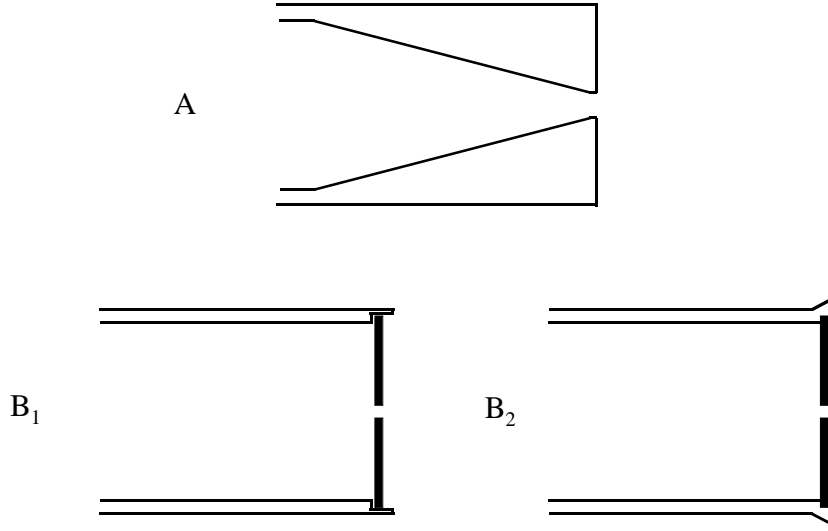


Figure 1.3: Schematics of both types of nozzles considered in this work. A: (ideal) conical nozzle, and B: (real) cylindrical nozzle. On the left, nozzle and aperture disk before final assembly, and on the right, drawing of a finalized nozzle, with the aperture disk clamp in place.

In order to facilitate the mathematical representation of the system, a rather crude simplification of the description of our nozzles is required: we must assume them to be both ideal, and conical. In *Atomic and Molecular Beam Methods* [44], a relation for the mass transfer  $\dot{m}$  when a gas is expanded from a pressure  $P_0$  into vacuum, through a conical nozzle is given as follows:

$$\dot{m} = P_0 A^* \left[ \frac{\gamma \omega}{RT_0} \left( \frac{2}{\gamma + 1} \right)^{(\gamma+1)(\gamma-1)} \right]^{1/2} \quad (1.3)$$

where  $P_0$  is expressed in Pa,  $A^*$  is the effective area of the aperture of the nozzle (in  $\text{m}^2$ ),  $\gamma$  is the ratio of the heat capacities (unitless, 5/3 for noble gases),  $\omega$  is the molar mass (in  $\text{kg mol}^{-1}$ ),  $R$  is the ideal gas constant ( $8.31451 \text{ J K}^{-1} \text{ mol}^{-1}$ ), and  $T_0$  is the expansion temperature (in K). This simple mathematical relation allows

one to predict the exiting gas flux from a few experimentally controlled variables.

The simplest way to determine the size of the aperture, is to measure the volume of gas expelled, at some known backing pressure, as a function of time (the term  $\dot{m}$  of equation 1.3). Then, knowing the properties of the gas and the expansion, we can easily get  $A^*$ , the area, and convert into a diameter. By fixing (arbitrarily) the volume collected to 2 ml, expanding from 40.0 psi above atmospheric pressure, and performing the experiment at room temperature (73.5 °F, or 296.2 K, in this case) we can obtain the following relation from equation 1.3 (after converting the area into a diameter with  $A^* = \pi \cdot (d/2)^2$ )

$$d = 2\sqrt{\frac{936.70}{\pi \cdot \Delta t}} \quad (1.4)$$

where  $d$  is the diameter of the nozzle, expressed in meter, and  $\Delta t$  is the time interval needed to collect the 2 ml of gas. The average of 10 runs gave us a diameter of 9.08  $\mu\text{m}$ .

Another use of this procedure is not only to diagnose clogged nozzles, but also to clean them since bubbling helium in ethanol, or any other ultra-pure solvent (spectroscopic grade is fine, no need to distill) usually dissolves contaminants (like diffusion pump oil) that stick to the outer face of the aperture disc and create recurring clogging problems.

## Prediction of the Beam Signal

Once the diameter of the nozzle is known, the flux (*prior* to condensation into droplets) for different backing pressures and temperatures can be predicted with equation 1.3. For example, to reproduce the beam conditions that were used in

Cloud II $\mathcal{E}$ , where the nozzle is also 10  $\mu\text{m}$  in diameter, we'd set  $P_0$  to 800 psi (1 psi = 6894.76 Pa), and  $T_0 = 16$  K, and find  $\dot{m} = 2.374 \times 10^{-6}$  kg/s. However, this value has to be corrected for the condensation efficiency: After the expansion, we can assume that *at least* 10% of the helium atoms condense into droplets, which brings the value down to  $2.4 \times 10^{-7}$  kg/s. Furthermore, one must consider the solid angle that “illuminates” the bolometer. In this machine, the distance from the expansion to the bolometer is about 350 mm, and the diameter of the round aperture of the bolometer mask is 3 mm. The solid angle  $\Omega$  (expressed in Sr, or steradian) is defined as the ratio of the area over the distance squared, *i.e.*

$$\Omega = \frac{A}{d^2} \quad (1.5)$$

which indicates that only one in  $2 \times 10^4$  ( $\Omega=6 \times 10^{-5}$ ) of the initial flux will make it to the detector, bringing down the value to  $1.6 \times 10^{-11}$  kg/s. For helium, at 4 g/mol, this value translates into  $4.05 \times 10^{-9}$  mol/s, or  $2.4 \times 10^{15}$  atoms/s. Each atom deposits 5/2 kT of (kinetic) energy on the surface of the detector upon impact, assuming an accommodation of 0.5 (the fraction of the energy which is effectively deposited on the detector: this value is, hopefully, not too far from reality), so the bolometer “sees”  $3.1 \times 10^{15}$  kT/s. At 16 K, kT is  $2.21 \times 10^{-22}$  J, so the power deposited on the detector is  $6.85 \times 10^{-7}$  W. The hydrogen bolometer has a detectivity of  $2.14 \times 10^5$  V/W, which allows us to predict a (conservative) beam signal of about 145 mV. The largest signal ever recorded is about 8.1 mV (see Fig. 1.4), about an order of magnitude below the estimate just presented. In terms of noise figure, the noise equivalent power (NEP) of the bolometer is  $1.3 \times 10^{-13}$  W/ $\sqrt{\text{Hz}}$  (for an intrinsic noise of 28 nV/ $\sqrt{\text{Hz}}$ ), so this predicted  $6.85 \times 10^{-7}$  W of power would show a signal-to-noise ratio (S/N) of about  $10^6$ . The best experimental noise value is about 70 nV/ $\sqrt{\text{Hz}}$ , so 8.1 mV of signal represents a S/N of  $10^5$ .

## Evaluation of the Performance of the Droplet Source

The performance of the improved helium droplet source is presented in figure 1.4. For a constant backing pressure of 800 psi, when going *down* in temperature, the bolometer signal decreases as the kinetic energy of the droplets decreases (linear in  $T$ ), even if the gas flux increases (only as  $\sqrt{T}$ ). The signal reaches a minimum value, between 40 to 33 K. At this point, the condensation into droplets may have started, but they are too small, and too few, to plow through the rather high gas pressure and survive past the skimmer. When condensation into droplets really picks-up, the signal starts increasing rapidly. The sharp increase (from 31 to 29 K in our case) corresponds to the onset of massive condensation. At this point, the bolometer signal fluctuates wildly, which may be the consequence of macroscopic fluctuations occurring at the phase transition [45]. The beam signal increases steadily as the droplets get larger and larger (the droplet size increases as  $T^{2.4}$ , the flux increases as  $\sqrt{T}$ , but the kinetic energy decreases as  $T$ ), until the large droplet limit is achieved (in our case, at 16 K). At that point, the cooling capacity of the closed-cycle refrigerators is reached and the system can no longer extract more heat from the incoming gas. According to the estimate of the flux calculated above, and setting the initial temperature of the incoming gas to 300 K, the power needed to precool the gas to 80 K is about 1.1 W. Then, in the second stage where the gas is then cooled from 80 K to the final temperature, 16 K, the thermal load is about 0.32 W. In both cases, the load can be easily handled by the cold heads, as the nozzle's cryocooler can supply *up to* 4 W at 20 K [46].

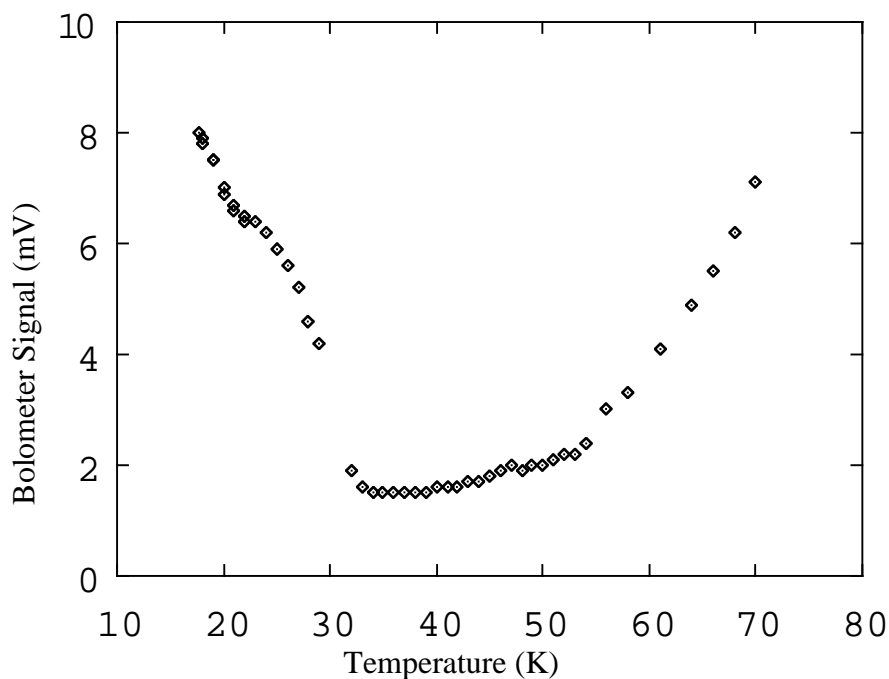


Figure 1.4: Temperature dependence of beam signal. Note the sharp increase of the signal at  $\sim 30$  K, where the onset of massive condensation occurs. The large droplet limit was reached at 16 K, where the cooling system gives up.

### The Oven/Pickup Cell

Because the primary use of this spectrometer is to study metal vapors embedded in helium nanodroplets, it is equipped with a pickup cell derived from a high temperature furnace [47] which can reach 1473 K due to the limitations of the present type-K thermocouple, the true limit of the device being 1773 K. To reduce infrared and visible radiation coming from the hot surfaces of the furnace (the bolometer is, by design, very sensitive to these wavelengths) a water-cooled copper shield was installed (see Fig. 1.5).

The shield features two 5 mm holes, the center of which are positioned about 2 mm above the edge of the furnace, to let the nanodroplet beam through

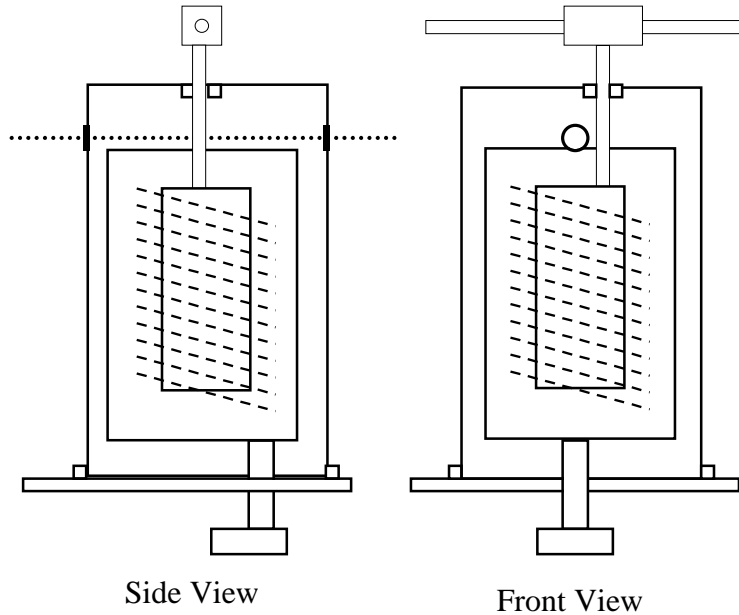


Figure 1.5: Schematic of the high temperature oven used as a pickup cell in Big Sur. The oblique dashed lines represent the tantalum wire (heating element), coiled around the small alumina crucible (small rectangle). The whole assembly is surrounded by a shielded housing, mounted on a stainless steel post. A copper plate, on which the water-cooled copper shield is resting, is clamped to the post. Side view: The droplet beam travels from the left to the right. Front view: The gas for pickup comes from the left arm of the “T”, while the right arm goes to a small Pirani gauge.

(see Side View, Fig. 1.5, the beam path is shown as a dotted line). The copper shield is 67.7 mm in diameter and extends 28 mm above the oven, thus forming a rather large pickup cell. On top of the shield, a hole has been drilled to position a high-temperature alumina tube that is used to leak the gas of interest at the *bottom* of the alumina crucible. The alumina tube is positioned to miss the droplet path, resting against the crucible wall. The bottom of the cell contains about 5 g of Fractalballs [48] that are useful for improving the contact time between the incoming gas and the hot crucible when the latter is used (not in the present experiments) to

crack heat sensitive molecules forming radicals by thermolysis. For the experiment described in chapter 2, the oven has been used as a standard (“cold”), pickup cell. The main disadvantage of this arrangement is that there is no means, at present, to read the pressure inside the cell. As shown on Fig. 1.5, the pressure is read “on top” of the gas inlet. From the conductance of the alumina tube that goes to the bottom of the oven, we can estimate that the pressure drops by at least two orders of magnitude from the top of the “T” to the bottom of the crucible.

### 1.1.3 Cloud II<sub>ε</sub>

This spectrometer has been described extensively in Ref. 21, and only the relevant details will be presented here. The single major change to this system was the replacement of the 5 μm nozzle by one with a 10 μm aperture to minimize clogging problems. Typical stagnation pressures used are around 800 psi (~ 5.5 MPa). After passing through a 500 μm skimmer located about 10 mm from the tip of the nozzle, the droplet beam is seeded in a 25 mm long gas pickup cell. Further downstream, the seeded droplet beam either travels coaxially through a section of waveguide (for the microwave experiment, see Sec. 1.3), or enters, perpendicular to it, an optical resonator (or buildup cavity [49]). In both cases, the droplet beam depletion is monitored thermally *via* phase sensitive thermal detection by a liquid–helium–cooled bolometer. This bolometer, unlike the one described previously (Sec. 1.1.2) is optimized to operate below the λ point of helium, at about 1.6 K. According to the manufacturer [50], it features a detectivity of  $7.7 \times 10^5$  V/W, and a noise equivalent power of  $4 \times 10^{-14}$  W/√Hz (the intrinsic noise is 31 nV/√Hz). This bolometer is also equipped with a JFET preamplifier (see Section 1.1.2 and Ref. [21]) so the performance of the device is close to the specifications of the manufacturer, even

with compressors and cold heads running. Following a calculation similar to the one presented in Section 1.1.2, for Big Sur’s nozzle, we can estimate that under standard experimental conditions (nozzle temperature of 20 K, backing pressure of 800 psi, and a solid angle of  $1.2 \times 10^{-5}$ ) about  $4.3 \times 10^{14}$  atoms/s hit the detector (for a predicted beam signal of about 120 mV). From the best beam signal ever recorded of about 5.5 mV, and the detectivity given above, we estimate the helium flux to be  $\sim 10^{13}$  atoms/s.

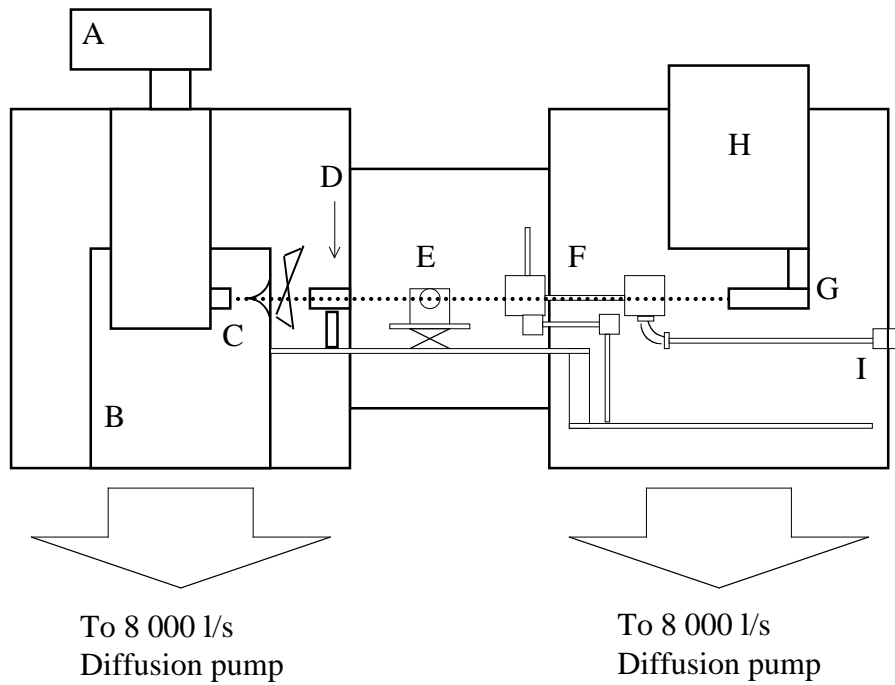


Figure 1.6: Diagram of Cloud II <sub>$\mathcal{E}$</sub> . A: cooler for the nozzle (pre-cooler not shown), B: the expansion chamber, which has a dedicated 8 000 l/s diff. pump, C: nozzle, located in front of the skimmer, D: pickup cell, E: build-up cavity, on vertical translation stage, F: microwave guide assembly (see Fig. 1.13), G: the bolometer and its cryostat H, and finally I: the microwave feedthrough.

## 1.2 Ultraviolet/Visible Spectroscopy

This section will first describe the laser setup, a state of the art, diode pumped Indigo Ti:Al<sub>2</sub>O<sub>3</sub> laser used to generate ultraviolet radiation for the photolysis experiment. Then, a description of the beam depletion experiments will be provided, before closing with a discussion of the fluorescence collection setup.

### 1.2.1 Introduction

From fancy state-selective dissociation to brute-force multiphoton processes, the study of laser photolysis has always been driven by technological advances, especially since the recent development of super-intense sub-femtosecond lasers. For the chemist, interest in photodissociation processes arises from the ease of *selectively* fragmenting molecules. Many radicals are formed *via* photolysis, as their bond energy is easily attainable with common lasers. The typical energy needed to break a chemical bond is of about 2–5 eV (200–500 kJ/mol): very weak bonds like the NN single bond in N<sub>2</sub>O<sub>4</sub> need about 0.6 eV (57 kJ/mol: this is *very* weak, and at room temperature, N<sub>2</sub>O<sub>4</sub> exists in equilibrium with NO<sub>2</sub>, with an equilibrium constant of  $1.72 \times 10^{-1}$  bar), whereas very strong bonds, like the NN triple bond require about 9.8 eV (945 kJ/mol for N<sub>2</sub>). In terms of laser “color”, the radiation needed to dissociate N<sub>2</sub>O<sub>4</sub>, would be in the infrared, around 4700 cm<sup>-1</sup>, and for N<sub>2</sub>, in the deep ultraviolet (DUV), at 79 000 cm<sup>-1</sup>. For the molecule considered here, NO<sub>2</sub>, with a NO–O dissociation energy of 25 128.57 cm<sup>-1</sup> (3.1 eV, or 300 kJ/mol), the radiation needed is at the boundary between the visible (blue) and the UV. Luckily, this wavelength range is easily accessible with modern lasers like the one described in the following section.

### 1.2.2 The Evolution X/Indigo Laser System

The experiments described in chapter 2 were made possible by the high performance of a novel state of the art, tuneable, high repetition rate, narrow linewidth, titanium sapphire ( $\text{Ti}:\text{Al}_2\text{O}_3$ ) laser system developed by Positive Light [51]. The unit bought by the Princeton group is the first of this new laser series, and at the time of purchase was still under development at Positive Light. In the prototype configuration in which the Indigo was received, tuning was not correctly implemented as the multiple elements forming the laser cavity could not be walked together during scanning. Instead of smoothly varying the wavelength of the emitted radiation, the laser was “mode hopping”: the wavelength was stepped in increments of 800 MHz (about 8 times the laser linewidth), which is unacceptable for spectroscopic purposes. In order to make the laser comply to our experimental requirements, several modifications had to be performed. Improvements to the Indigo  $\text{Ti}:\text{Al}_2\text{O}_3$  laser were done by Roman Schmied, as part of his master thesis [52], with some help from the group and the staff at Positive Light.

The  $\text{Ti}:\text{Al}_2\text{O}_3$  medium, up to 0.35%  $\text{Ti}^{3+}$  ions embedded in a sapphire crystal, can generate light over a very broad range, from 660 to 1100 nm, with maximum efficiency around 800 nm. Its maximum absorption is at 490 nm, which makes it ideal to use as pump lasers the new ultra-quiet diode-pumped near-IR lasers which, when doubled, deliver vast amounts of power, and high mode quality, around the absorption maximum (for example: 527 nm for Nd:YLF, and 532 nm for Nd:YAG). The Positive Light laser system uses a 10 W, 1 kHz repetition rate Nd:YLF laser, the Evolution X. It is a Q-switched, intracavity doubled laser pumped by four AlGaAs diode arrays. Its high mode quality allows the associated tuneable near-infrared  $\text{Ti}:\text{Al}_2\text{O}_3$  laser, the Indigo, to generate near transform limited, 10 ns

pulses of energies up to 1.7 mJ (or 1.7 W at 1 kHz), with high pulse-to-pulse stability. The cavity layout of the Indigo is shown in figure 1.7. It is a modified Fox-Smith resonator consisting of three mirrors and a grating forming two coupled cavities. The lasing efficiency and output quality of this laser are provided by these two coupled cavities: one for power buildup and the second for wavelength selectivity. Light from the pump laser enters the main cavity near the high reflector M1, hits the crystal and reflects off the grating at grazing incidence (about  $1.5^\circ$  in this setup). 30% of the incident power bounces back off the output coupler M2 (the remainder is transmitted) and careful alignment insures that the red light is directed towards the high reflector instead of following the path of the incoming green light. This cavity, when isolated (*i.e.* without the grating), produces broadband emission with high efficiency. The secondary cavity takes light from the first order diffraction off the grating and bounces it back and forth between the tuning mirror and M1 (*via* the grating). This secondary cavity is very wavelength selective, and seeds the main cavity thus forcing the crystal into lasing in a narrow-band single-mode.

Our setup features two sets of M1 and M2 mirrors (see Fig. 1.7): A mid-band set, optimized for operation from 760 to 830 nm, and a short-band set that allows to go as low as 736 nm. Using a LBO doubling crystal (lithium triborate,  $\text{LiB}_3\text{O}_5$ : a matrix of  $\text{B}_3\text{O}_7$  with  $\text{Li}^+$  filling the interstices), blue/UV light can be produced with single-pass efficiencies of more than 10%. The output pulse energy, in the blue, can be maintained well over 200  $\mu\text{J}$  (200 mW at 1 kHz repetition rate), with both sets of optics. The Indigo can also be equipped with a tripler, that adds the blue to the red (better conversion efficiency than direct tripling can in this way be achieved) and a quadrupler that works under the same principle as the tripler, by adding the red to the tripled light instead of doubling the blue. At this time, neither the tripler nor the quadrupler have been tested.

The general layout of the Indigo is shown in figure 1.8. The pump beam is first telescoped, and then tightly focused on the Ti:Al<sub>2</sub>O<sub>3</sub> crystal. Upon exiting the lasing cavity, the near-IR output can either be used directly (with the flip mirror down), or be used to pump the doubling crystal (with the flip mirror in position). The near-IR is tightly focused on the crystal in order to achieve the required high electromagnetic fields, providing efficient single-pass conversion. The Blue/UV light is then collimated with the second element of the telescope T<sub>2</sub>, and guided out of the laser with dichroic mirrors.

### 1.2.3 Multi-Pass Cell and Beam Depletion

In contrast with the high-resolution infrared experiment previously conducted in the Scoles group, where the laser radiation is amplified by means of a resonant cavity (or buildup cavity, BUC, see Ref. [49]), the ultraviolet experiment makes use of a more traditional, and somewhat simpler, multipass cell. The main reasons for this choice is that no mirror of sufficiently high reflectivity exists for the *whole* wavelength region

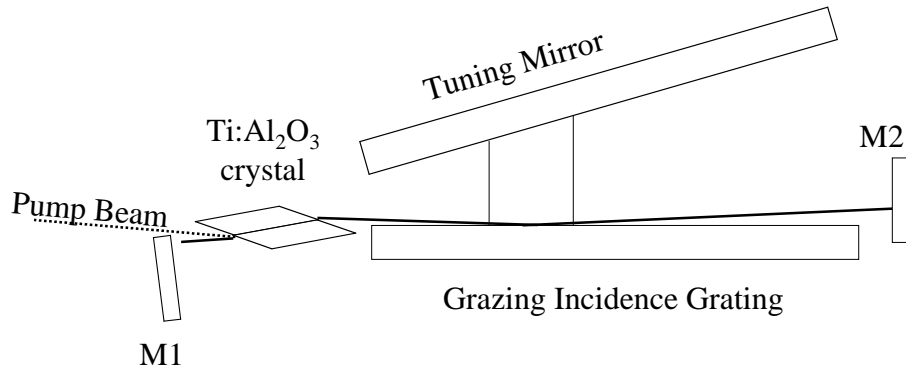


Figure 1.7: Simplified diagram of the Indigo laser cavity. M1 is the high reflector; M2 is the output coupler (about 30% reflectivity). The different paths for the pump beam going to the crystal, and the transmitted near-IR light going to M1 are due to the high index of refraction of the lasing medium ( $n = 1.8$ ).

where we needed to work, namely 405 to 345 nm. Also, efficient coupling of a pulsed source to a BUC is rather difficult. Dielectric mirrors are available, but their rather narrow range of high reflectivity makes the buildup cavity design inconvenient, since several setups would be necessary to cover the wavelengths of interest. Furthermore, the linewidth of the laser (100 MHz, on a good day) is about 100 times larger than the linewidth of a reasonably fine cavity ( $f \sim 10\,000$ ), which is on the order of 1 MHz for a free spectral range of 10 GHz. Thus, even if wide bandwidth, high reflectivity mirrors were available, the efficiency of the system would be very low, as most of the laser power would be off-resonance with the cavity mode being pumped. The multipass cell offers a very acceptable “buildup” (about 40-46 passes, depending on the quality of the alignment, only a factor of 10 lower than the BUC), without the need for fancy optics and electronics to further stabilize the laser, and lock the

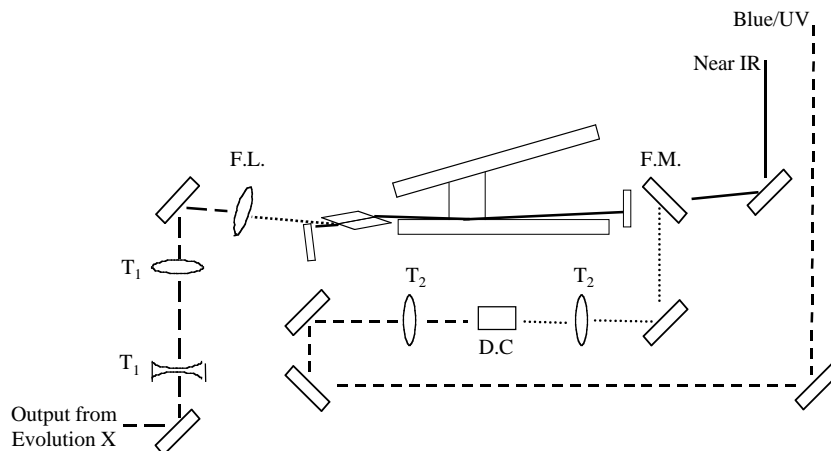


Figure 1.8: Layout of the internal components of the Indigo. Shown is the path of the near-IR (solid line) and the doubled (UV) radiation (dashed line).  $T_1$  the pump beam telescope, F.L. a focusing lens, F.M. a flip mirror for selecting the output,  $T_2$  the doubler telescope elements, and D.C. the doubling crystal. Recognize the Fox–Smith cavity from Fig. 1.7.

cavity to the laser. Scanning is thus easier, and faster, since it is only limited by the data acquisition rate (in most cases).

Instead of building a traditional multipass cell, where two mirrors are perfectly parallel to each other, two 14' wedges have been used as spacers (exactly 0.0062", or 0.16 mm, has been progressively ground over the 40 mm length of the spacers). This small angle between the mirrors (the "thick" part at the entrance) allows the laser beam to enter the cell, bounce back and forth until the edge of the mirrors, where it comes back on itself, moving back towards the entrance of the cell where it exits the setup. A *very* simplified drawing is presented in Fig. 1.9. The

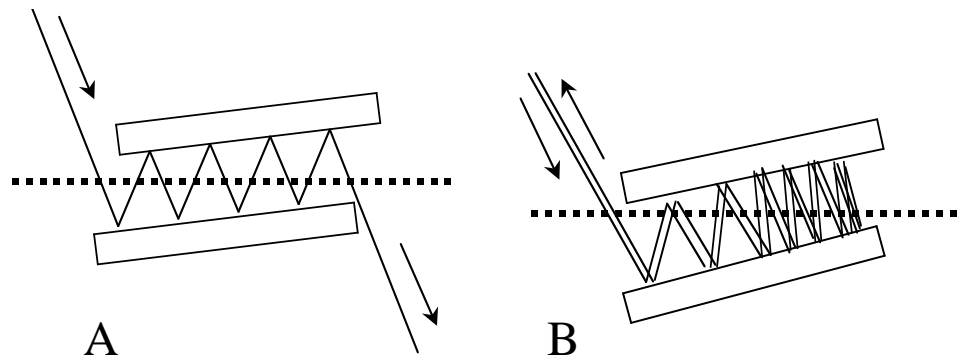


Figure 1.9: Schematic of multipass cells. A: With perfectly parallel spacers, and B: with wedged spacers. Both are seen from the top, as if looking through transparent spacers (the rectangles are the high reflectivity mirrors). In both pictures, the droplet beam path is shown as a dotted line.

main problem with the wedged spacers setup, is that the horizontal alignment of the spacers is *critical*. In fact, if the mirrors aren't perfectly positioned with respect to each other, it is nearly impossible to get the laser beam to travel in a straight line, parallel to the nanodroplet beam. Instead, it follows a curved path which can deviate by as much as 10 mm from the estimated position (see Fig. 1.10).

By varying the entrance angle of the multipass cell, with respect to the

laser beam, one can maximize the number of reflections, optimizing the interaction between the laser and the droplet beam. A value of 42 passes can be easily be attained (in fact, the number of passes is most often limited by one’s ability to count the spots towards the end of the cell, where the laser comes back on itself!).

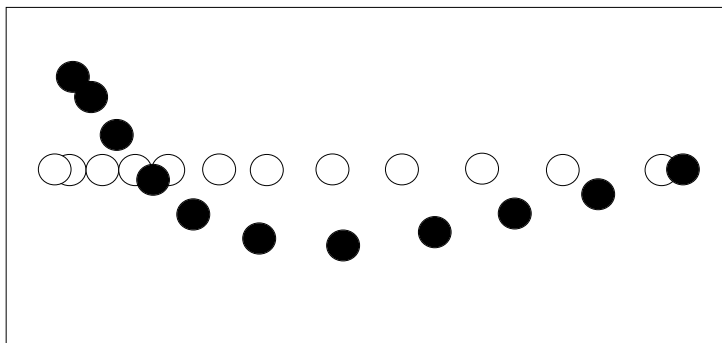


Figure 1.10: Schematic of laser beam reflected spots on the multipass cell mirrors. Open circles: spacers correctly aligned. Black circles: spacers misaligned. The return path has been omitted for clarity.

#### 1.2.4 Fluorescence Collection

The fluorescence collector used for these experiments is the same that has been used in the past in our laboratory [53, 54]. It is shown in figure 1.11 A. It features two mirrors, one spherical (S), and one elliptical (E). The elliptical mirror focuses any “ray” of light emitted from the center of the cell (one of its focal points) on the second focal point, which is located on the surface of the spherical mirror, where the entrance of the fiber bundle is located. The spherical mirror reflects all beams through the center of the cell, and then the elliptical mirror takes care of reflecting it on the fiber. Light going to the elliptical mirror first gets to the fiber after one pass, whereas light going towards the spherical mirror is reflected one more time

(unless, of course, it enters the fiber directly).

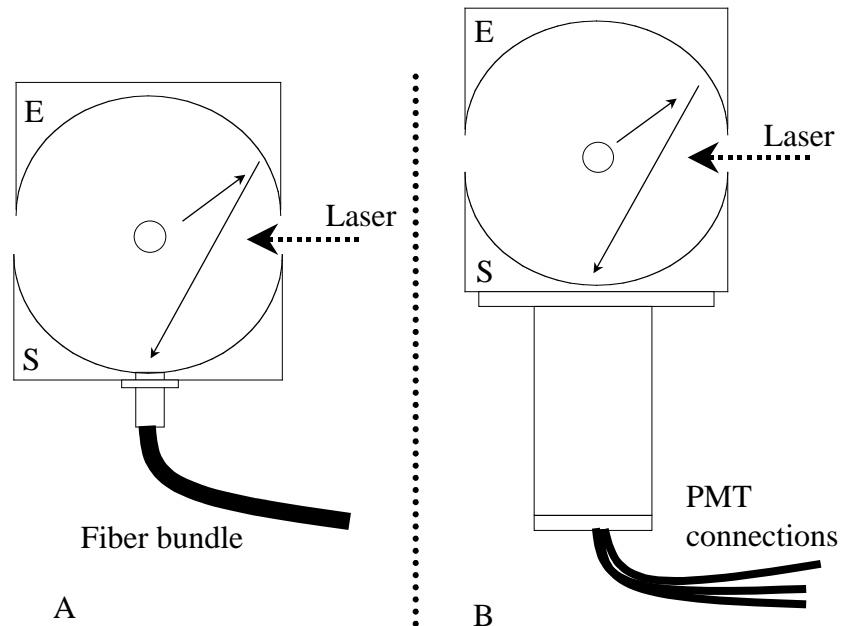


Figure 1.11: Diagram of the fluorescence collector. A: with fiber bundle installed, and B: with small PMT attached directly underneath. The circle in the middle represents the position of the droplet beam. The PMT mount features a groove to allow room for a standard, 2" diameter Andover Corp. filter [55].

In order to enhance the performance of the photon collection system at short wavelength, a compact, vacuum-compatible, PMT was purchased [56] (see Fig. 1.11 B). Instead of bringing the collected photons outside of the machine, through a fiber bundle, to be detected, the new PMT allows the photons to be counted in vacuum, thus eliminating the lossy bundle and further improving the collection efficiency with a better acceptance angle. Furthermore, its sensitivity curve is rather high at wavelengths as low as 200 nm, where the responsivity is  $7 \times 10^3$  A/W. The current PMT [57] only offers  $1.8 \times 10^3$  A/W at 420 nm: by 500 nm, the response drops *very* sharply. A second logical step in improving the

overall performance of the system is to increase the field intensity at the interaction zone, in order to enhance the excitation efficiency. To achieve this, the collector setup has been modified to accommodate a focusing lens at the entrance of the laser beam. The lens is clamped between the inner edge of a Delrin retaining sleeve and a Delrin spacer (See Fig. 1.12). The spacer is put against the end of the brass tube (containing a set baffles designed to minimize scattered light from the incoming laser beam). The thickness is determined experimentally to fine-tune the position of the focus exactly at droplet beam. Using a  $f = 100$  mm focal length lens of 25.4 mm diameter [58], the diffraction limited spot size  $\omega$  can be obtained from the following equation

$$\omega = \frac{f\lambda}{\pi\omega_0} \quad (1.6)$$

where  $\omega_0$  is the waist of the incoming laser beam (the radius). For a waist of 0.5 mm (a long focal length lens situated right outside of the laser reduces the laser divergence to maintain a beam diameter of about 1 mm), at 400 nm, with our  $f = 100$  mm lens, the spot size (twice the waist  $\omega$ ) would be 50  $\mu\text{m}$ . Note that this equation does not take into account spherical aberrations, or other non-idealities, which *must* be taken into account when spot sizes on the order of 10  $\mu\text{m}$ , or smaller, are expected: in our case, they can be neglected.

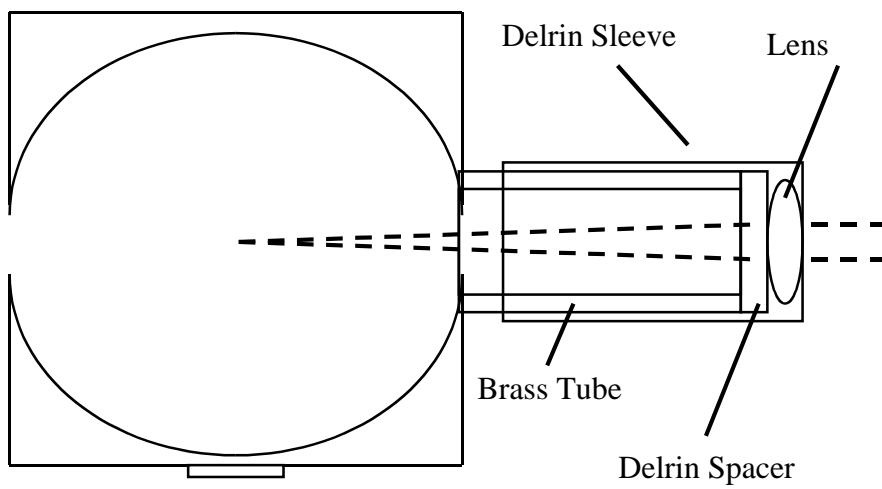


Figure 1.12: Diagram of the lens mount assembly for tight focusing the excitation laser at the center of the LIF collector. The light path is shown as a dotted line (the size of the laser beam is grossly exaggerated for clarity).

## 1.3 Microwave Spectroscopy

Gas phase microwave spectroscopy allows the study of the structure of molecules from their rotational properties. From the rotational constant  $B$ , which is related to the moment of inertia  $I$  (which is itself a function of the reduced mass  $\mu$  and the equilibrium distance  $r_e$ ) *via* the following relation

$$B \text{ (GHz)} = \frac{505.38}{I \text{ (amu} \cdot \text{\AA)}^2} ; I = \mu r_e^2 \quad (1.7)$$

spectroscopists have been able to determine molecular structure very accurately (with modern techniques, bond lengths can be determined to within a few tenths of a percent, limited only by the correction terms for the vibrational effect on the rotational constants [59]). For species embedded in helium nanodroplets, pure rotational spectroscopy is an important complement to infrared spectroscopy, as it permits the elucidation of relaxation mechanisms, without considering vibrational effects. This section will describe the experimental setup used to measure the microwave spectra of small, isotopically substituted molecules embedded in helium nanodroplets.

### 1.3.1 Introduction

Several pure microwave experiments have been performed in the past. The group has studied (MW) single- and (MW-MW) double-resonance spectra of cyanoacetylene. Important results leading to the identification of the main line broadening mechanism in HENDI spectroscopy were obtained [33], and the lifetime of rotational excited states could be inferred, which confirmed the importance of pure rotational spectroscopy for purposes other than structure determination. A very special fea-

ture of HENDI MW spectroscopy is related to these short (tens of ns) lifetimes. As the photon energy is very small ( $2.5 \text{ cm}^{-1}$  at 75 GHz), beam depletion detection must rely on the absorption of *several* photons to generate a measurable signal. This issue will be discussed in section 1.3.3, but first, the microwave generator and the necessary hardware will be described.

### 1.3.2 Sweeper and Multiplier Head

The microwave radiation is produced by a synthesized sweeper (HP 83752B, 0.01 — 20 GHz) coupled to a frequency quadrupler (millimeter wave source module HP 83557A, 50–75 GHz, with V-band waveguide output) capable of generating up to +12.3 dBm, or 17 mW of microwave power (only +9.3 dBm, or 8.5 mW, can be used when running the multiplier in “level” mode, thus insuring that the power is constant over the whole scanning range of the device). The MW synthesizer is amplitude modulated at  $\sim 310 \text{ Hz}$  for lock-in detection. All critical parameters (MW frequency, power, modulation frequency and amplitude) are internally controlled by the MW synthesizer to specifications exceeding the requirements of the present experiment.

### 1.3.3 Waveguide and Detection of Beam Depletion

After the center portion of the beam is extracted by the skimmer, (see Section 1.1.3), the nanodroplets pass through a 10 cm long Q-band waveguide (nominal range 33–50 GHz) which is aligned parallel to the cluster beam, as shown on Fig. 1.13, item C. Although a V-band (nominal range 50–75 GHz) would have been more appropriate for optimum propagation of the microwave radiation, this lower frequency wave-

uide was chosen because of its larger dimensions ( $5.7 \times 2.8 \text{ mm}^2$ ) to minimize alignment problems. The radiation is coupled in and out of the waveguide through two 2.8 mm ( $7/64^{\text{th}}$ ) diameter holes in the E-bends, items B at both ends of the guide; a microwave dump (VSWR=1.03:1) at the exit end, item A, minimizes reflections back into the waveguide, thus preventing occurrence of an unwanted standing wave pattern. The microwaves are coupled to the vacuum system with flexible Q-band waveguide mated to the curved part D through a thin layer of mylar, squeezed between two o-rings to insure an vacuum-tight seal (the multiplier head is coupled directly to a V-band/Q-band adaptor). This setup is preferred to a more flexible high frequency coax and SMA feedthrough in order to minimize power losses both through the cable and at the coax/waveguide junctions.

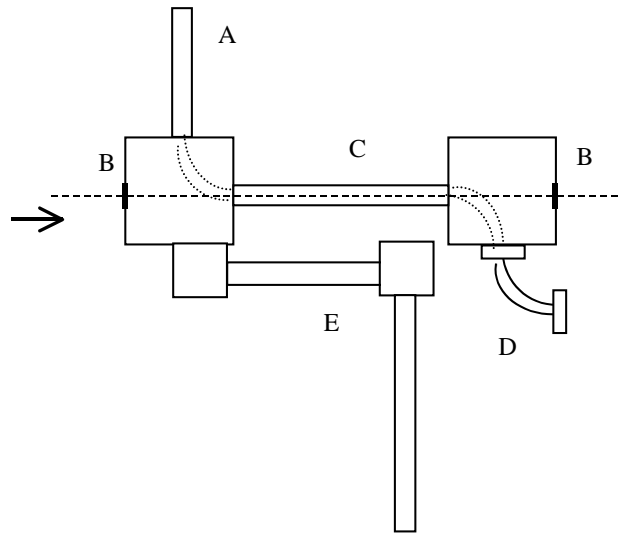


Figure 1.13: Schematics of the microwave cell installed in Cloud II $\mathcal{E}$ . A: wave dump, B: two E-bends, C: Q-band waveguide, D: curved Q-band waveguide to interface to the feedthrough (not shown), and E: mounting hardware allowing height, and tilt adjustments. The arrow on the left indicates the direction of the travel of the nanodroplet beam

Multiple successive resonant photon absorption and energy relaxation by

the rotor in the droplet “bath”, leads to evaporation of He from the droplet. The depletion signal is detected as decrease of the droplet signal by a liquid–helium–cooled silicon bolometer (see Section 1.1.3) *via* phase sensitive detection with a lock–in amplifier [41] equipped with the manufacturer’s preamplifier [42]. To reach signal levels comparable to those obtained in the infrared experiments reported previously [20], we estimate that about 3000 absorption–relaxation cycles must occur during the transit time through the waveguide (to deposit the same amount of energy as a  $6600\text{ cm}^{-1}$  IR photon, at a microwave frequency of 70 GHz). Estimating the nanodroplet velocity to be 450 m/s, the transit time is of about 200  $\mu\text{s}$ , which implies that the relaxation must be faster than 70 ns. This estimate will prove to be rather accurate, as the experimentally determined values of the relaxation times  $T_1$  and  $T_2$ , on the order of 20 ns, will be discussed in Chapter 3.

## Chapter 2

# Formation of Highly Reactive Species From Embedded Impurities: Photolysis of NO<sub>2</sub>

*“There are numerous scientific benchmark systems that people return to — as pilgrims to Mecca — seeking knowledge and testing their comprehension of the world around them. They include hydrogen in quantum physics, drosophila DNA in genetics, and the value of  $\pi$  in arithmetics. For gas phase chemical physics, NO<sub>2</sub> could be such a system.” [60]*

This chapter will report the first attempt to generate highly reactive species (in this case, the O and NO radicals) from the photodissociation of stable, neutral molecules (NO<sub>2</sub>) embedded in helium nanodroplets. Firstly, the NO<sub>2</sub> molecular system will be presented, and its dynamics of dissociation into O and NO, will be described. Secondly, the experimental procedure, and the data, will be presented for

both the beam depletion and the fluorescence experiments. Beam depletion data show no sign of dissociation, up to  $2000\text{ cm}^{-1}$  beyond the gas phase dissociation threshold. Cooling of the vibronically excited molecules can, in principle, explain our fluorescence data; a lower limit for the cooling rate of vibronically excited  $\text{NO}_2$  in helium can be determined. However, different cooling mechanisms are proposed, and their compatibility with experimental data will be discussed. The description of an experiment designed to probe the appearance of NO in the droplets, if it is temporarily formed during the excitation process, will close the chapter.

## 2.1 Introduction

The idea of synthesizing novel compounds from matrix isolated precursors is not new, and several methods have been proposed to generate the active reactant. In the “first” matrix isolation paper, Pimentel and collaborators pointed out that:

“The active material can be produced in a variety of ways: by chemical reaction involving two reactants, by pyrolysis, by dissociation in a glow discharge or an arc, or by photolysis. Only the last permits forming the active molecule *after* the trapping process has been carried out. Otherwise, it is necessary to produce the active material and to trap it in the matrix shortly thereafter.” [7]

As in solid (rare-gas) matrices, the seeding of nanodroplets with radicals can be performed in two ways. Firstly, the radical can be produced, and then picked up by the beam of droplets. Efficient radical production from glow discharges has been reported in the literature, and the dynamics of such plasmas are well understood.

Unfortunately, the pickup of such species may not be easy: dissociation products may recombine on their way to the pickup box because of the relatively high pressures needed to sustain the discharge (about three orders of magnitude higher than the “usual” pickup pressures of about  $10^{-4}$  Torr). Furthermore, the pickup dynamics of such “hot” molecules may differ from that of room temperature neutrals, as the droplets need to dissipate a lot more energy upon solvating the guest. Overall, the advantages of generating radicals in a well known and controlled manner may well be outweighed by the difficulty of picking them up. The second alternative is to first pick up a precursor known to yield the desired product efficiently, and then form the radicals *in situ*, *via* photolysis. The idea of forming the active species after trapping the precursor in helium is very attractive, as the pickup of neutral molecules is easy, and well understood [2, 12]. Furthermore, preliminary spectroscopic analysis can be performed on the precursor such that all the expansion and pickup parameters can be optimized prior to attempting the photolysis. Additionally, following the photolysis of a neutral into two radicals, there is a possibility that a novel van der Waals complex could be created from the combination of the fragments, as the low temperature of the bath may keep them from chemically recombining into the original precursor. This may occur for one of two reasons: either an irreversible spin transition into a high spin state or because of the existence of a (albeit small) barrier to recombination.

The electronic spectroscopy of  $\text{NO}_2$  has been studied for years, as the molecule has been a “benchmark system” for many experiments. Therefore, an electronic spectrum of  $\text{NO}_2$  embedded in helium is likely to be of interest to the scientific community. Thus, even the preliminary phase of the experiment, the optimization of the pickup by observation of the spectrum of  $\text{NO}_2$ , offers a potentially important contribution to the field.

The photolysis of  $\text{NO}_2$  is also of considerable interest though for a different reason: its dissociation products  $\text{NO}$  and  $\text{O}$  are highly reactive species which have attracted a lot of attention in recent years. The oxygen diradical is a very strong oxidant. In its ground state,  $^3P_{2,1,0}$ , it reacts without barrier with unsaturated organic molecules (for example acetylene and ethylene [61, 62]); it even reacts with the more inert saturated hydrocarbons, *via* hydrogen atom abstraction with a modest barrier (ethane gives 1.9 kcal/mol, see Ref. 63).  $\text{NO}$ , nitric oxide, has long been a prototype for a stable radical species. Its primary atmospheric source is the combustion of fossil fuel and it is associated with the formation of ozone in the troposphere. It is often a target in spectroscopic measurements involved in combustion diagnostics.  $\text{NO}$  is also of great industrial importance as a precursor in the mass production of nitric acid, and as a stabilizer (a scavenger, to prevent free-radical decomposition) for molecules such as propylene and dimethyl-ether. Last but not least,  $\text{NO}$  is implicated in a wide range of biological processes. Since  $\text{NO}$  is a rather toxic free radical gas, it is (somewhat of) a surprise that the molecule may function as an intercellular signal in regulating blood vessel dilation, serve as a neurotransmitter, and also function in immune response. Unsurprisingly,  $\text{NO}$  became the molecule of the year in 1992: “A startlingly simple molecule unites neuroscience, physiology, and immunology, and revises scientists’ understanding of how cells communicate and defend themselves” [64]. Consequently, the photolysis of  $\text{NO}_2$  embedded in helium nanodroplets is worth pursuing for two reasons: to further our understanding of the dissociation process itself, by adding to the current knowledge the contributions of solvation, and to devise an efficient method of producing chemically relevant radicals, and move towards taking full advantage of HENDI in the synthesis and interrogation of novel molecular species.

## 2.2 Electronic Excitations of NO<sub>2</sub>

We attempted to photodissociate NO<sub>2</sub> into an oxygen atom, and NO *via* a standard one-photon process around 398 nm. The dynamics of this photolysis reaction is well studied: Several experiments succeeded at observing the unimolecular decomposition both in the gas phase and in supersonic jets. Owing to the features of jets, and the ever increasing resolution of laser induced fluorescence (LIF) experiments, the value of the gas phase dissociation threshold is known very accurately to be  $25\,128.57 \pm 0.05 \text{ cm}^{-1}$  [65]. Unfortunately, the dynamics of the process leading to dissociation are not so well known, eventhough a number of experiments have studied the electronic structure of NO<sub>2</sub>. The landmark paper by Gillispie *et al.* [66] has established that the extremely dense spectroscopy of this molecule was due to a conical intersection between the  $\tilde{X}^2A_1$  ground state, and the first excited state,  $\tilde{A}^2B_2$ .

The electronic system of NO<sub>2</sub> is very rich and its visible spectroscopy is complex, with most of the features being induced by strong coupling between the  $\tilde{X}^2A_1$  ground state, and the first excited state  $\tilde{A}^2B_2$ , whose origin is located  $9737 \text{ cm}^{-1}$  above the minimum of the ground state potential. The most striking feature of NO<sub>2</sub>, when approaching the dissociation threshold, is that starting around  $17\,000 \text{ cm}^{-1}$  (2/3 of the way up), the  $\tilde{X}^2A_1$  and  $\tilde{A}^2B_2$  electronic states are *completely* mixed into a vibronic manifold of  $A_1/B_2$  symmetry, with only half the states (those of  $B_2$  symmetry) being optically accessible from the ground state. Around  $23\,000 \text{ cm}^{-1}$ , further mixing provides bright character to the (originally dark)  $A_1$  vibronic species and the system displays what is called rovibronic chaos. This effect is induced by very strong intramolecular interactions, and is unexpected for such a small molecule whose density of vibronic states of  $B_2$  symmetry is rather sparse, at most on the

order of  $2.7/\text{cm}^{-1}$  [65, 67]. The observed (*i.e.* optically bright) density of states, the *density of transitions* is  $16/\text{cm}^{-1}$  (six times higher), as four transitions originating from the  $J = 3/2$  state, and two from the  $J = 1/2$  state, can be observed, because of complete mixing of the states with the same vibronic  $B_2$  symmetry.

## The Conical Intersection

The ground electronic and vibrational wavefunctions of  $\text{NO}_2$  are of  $A_1$  symmetry (fully symmetric representation of the  $C_{2v}$  point group), and the first excited state has  $B_2$  symmetry<sup>1</sup>.  $\text{NO}_2$  has three vibrational modes ( $3N - 6$ ), two of  $a_1$  symmetry (symmetric stretch and bend) and one of  $b_2$  symmetry (asymmetric stretch). Above the conical intersection, the vibronic states of  $B_2$  symmetry can be built of  $a_1$  vibrational modes, or an *even* number of quanta in the  $b_2$  vibrational modes, in the  $B_2$  electronic state, or an *odd* number of quanta in the  $b_2$  vibrational mode in the  $A_1$  state. In the Frank–Condon region, the two electronic states are coupled *via* the asymmetric stretch ( $b_2$  symmetry). Since strong coupling between the two surfaces mainly occurs *at* the conical intersection, known to occur at an angle of  $107.4^\circ$  (the ground state equilibrium geometry has a bond angle of  $134.1^\circ$ ) the excited molecule stays on the  $B$  surface for the time of about one bending mode period. In other words, coupling between the electronic surfaces arises since the asymmetric stretch breaks the  $C_{2v}$  symmetry into  $C_s$ , and the  $A_1$  and  $B_2$  collapse into the same representation,  $A'$ . Consequently, species having different vibrational and electronic symmetry, but the same vibronic symmetry are strongly mixed, forming a manifold of  $A_1$  and  $B_2$  vibronic species, with only the  $B_2$  states being *optically* accessible.

---

<sup>1</sup>In this discussion, the representations of electronic states will be shown in uppercase, whereas the representations of vibrational modes will be shown as lowercase.

## Below the Dissociation Threshold

Below the dissociation threshold, the isolated molecule can only relax *via* fluorescence, as the excited states created on a manifold of  $A_1$  and  $B_2$  symmetry vibronic levels cannot decay nonradiatively *via* the ground state. Such an excited state will decay rather slowly, within a few  $\mu\text{s}$ : Fluorescence will occur exclusively from states with  $B_2$  vibronic symmetry into  $a_1$  states of the  $A_1$  electronic state, or from states with  $A_1$  vibronic symmetry into  $b_2$  vibrational states of the  $A_1$  electronic state: this corresponds to half the levels of the mixed electronic system (see Fig. 2.1). As the energy of the excited state approaches the dissociation threshold, however, rovibronic interactions start to couple more levels with  $A_1$  symmetry, and the system displays more rovibronic character, leading eventually to rovibronic chaos. Recent experiments [68] have also suggested that *very* close to (but still below) the threshold, a family of states corresponding to the large amplitude motion (occurring at interfragment distances larger than about 7 Å) of an O atom around the NO molecule, may exist. This hypothesis arose from the observation of a striking analogy between the spectral features of  $\text{NO}_2$  near the threshold, and the spectra of weakly bound (for instance,  $\text{NO—Ar}$ ) van der Waals complex [69]: In other words, a loosely bound  $\text{NO}_2$  molecule appears to have properties which are similar to those of a van der Waals complex (as most of the energy seems to be shared between the dissociation coordinate and the rotor, with no excitation localized in the NO fragment). The observation that, around  $20\text{ cm}^{-1}$  from the dissociation threshold, the density of states suddenly increases by a factor of about five [70] also corroborates this van der Waals complex analogy.

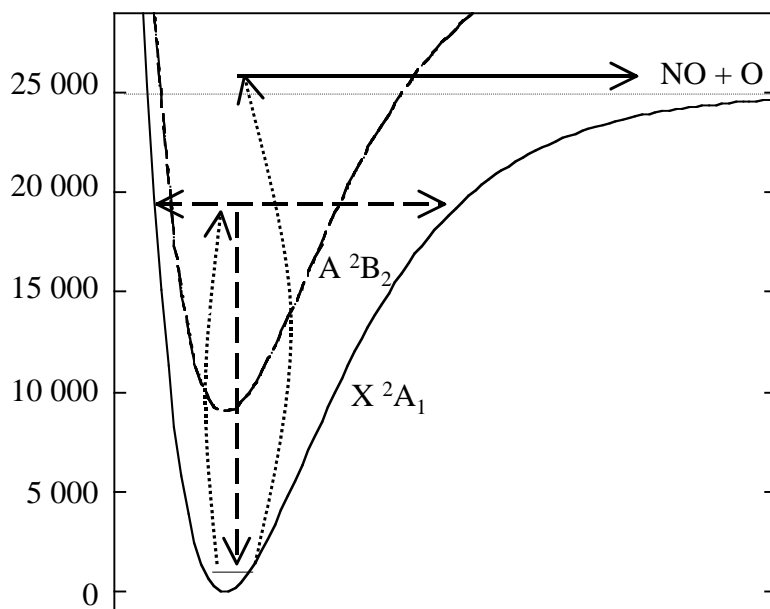


Figure 2.1: Picture of the two potential energy surfaces involved in the photodissociation process of  $\text{NO}_2$ . The molecule is first excited to the  $\tilde{A} \ ^2B_2$  state, and rapidly converts back to the  $\tilde{X} \ ^2A_1$  where it dissociates. Below the threshold, the excited state is “trapped” in the  $A_1/B_2$  manifold, and oscillate in the potential well until it decays *via* fluorescence from a vibronic state of  $B_2$  symmetry to the ground  $A_1$  vibronic state.

### Above the Dissociation Threshold

The dissociation of  $\text{NO}_2$  occurs on the *ground*  $\tilde{X} \ ^2A_1$  potential energy surface *via* a barrierless channel which leads to  $\text{NO}(X \ ^2\Pi_{1/2,3/2}) + \text{O}(^3P_{1,2,3})$  [71]. The molecule is first excited to the bright  $\tilde{A} \ ^2B_2$  state, and it then nonradiatively crosses back to the ground state within one asymmetric stretch vibrational period, subsequently dissociating within a tenth of a ns (see Fig. 2.1). As dissociation is more than four orders of magnitude faster than radiative relaxation, no fluorescence can be detected, and the threshold is observed as a sharp drop in the fluorescence signal intensity (more than three orders of magnitude over about  $0.25 \text{ cm}^{-1}$ , according to Ref. 65).

## **2.3 Droplet Beam Depletion Experiments with NO<sub>2</sub>**

### **2.3.1 Calibration Study of the Dependence of the Helium Beam Signal with Pickup Pressure**

This subsection will outline the results of an important calibration experiment, the variations of the droplet beam signal as the pickup pressure is increased. The results of this experiment will help in evaluating the efficiency of the pickup cell. In an ideal case, one would observe no depletion of the beam signal due to pickup alone (only the amount necessary to thermalize the guest molecule). Unfortunately, it is not the case; in order to make accurate predictions, one must understand the pickup dynamics. Figure 2.2 presents the effect of the pickup pressure on the beam signal. The nozzle was cooled down to the lowest possible temperature (16 K) and the backing pressure was 700 psi. Recall that the pickup pressure is measured not in the cell itself, but on top of the gas inlet (see Section 1.1.2). The large pressure gradient over the length of the inlet tube explains why the pressures shown in figure 2.2 are in the tens of Torr range instead of the tenths of mTorr range as is normally the case in our pickup cells.

### **2.3.2 Beam Depletion Near the Dissociation Threshold of NO<sub>2</sub>**

This experiment has been performed with the setup described in Section 1.1.2 and 1.2.3. The beam of doped nanodroplets interacts with the blue light (from

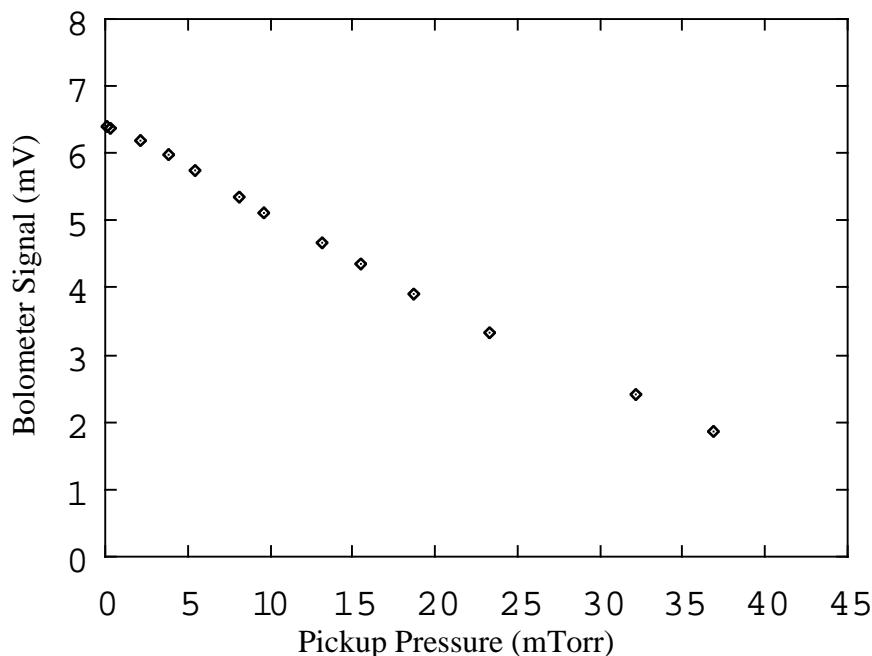


Figure 2.2: Variation of the beam signal with pickup pressure. The best  $\text{NO}_2$  signal is observed in the range 20–30 mTorr, where about half the beam signal is lost (see Sec. 2.3.2).

400 to 368 nm) in the multi-pass cell at a laser power of about 200 mW (measured right out of the laser). From the effective laser intensity of 162 mW, averaged over 42 reflections (and overestimating 1% loss each time) and the spot size ( $1 \text{ mm}^2$ ), knowing the absorption cross section of  $\text{NO}_2$  ( $6 \times 10^{-19} \text{ cm}^2/\text{molecule}$ ) and the flux of droplets (experimentally determined from the helium beam signal to be  $5 \times 10^9$  droplets/s, with *at most*  $1/e$  being doped with  $\text{NO}_2$ ), we can estimate that the optimal bolometer signal will be  $86 \mu\text{V}$ . As shown on Fig. 2.3, at the pickup pressure corresponding to the maximum molecular signal, the attenuation is *at least* 40% (see Section 2.3.1, Fig. 2.2), which decreases the estimated optimal  $\text{NO}_2$  signal to  $52 \mu\text{V}$ . We observed, on average,  $20 \mu\text{V}$  of signal (see Fig. 2.4), well within a factor of three from the estimate. In Fig. 2.3, the high pressure limit is set not by the disappear-

ance of the signal (as it should be), but by the vapor pressure of  $\text{N}_2\text{O}_4$  in a  $-72\text{ }^\circ\text{C}$  dry ice/ethanol cryogenic bath (less than 0.1 Torr: the vapor pressure is 1 Torr at  $-55.6\text{ }^\circ\text{C}$  [72]). The dry ice/ethanol mixture was chosen for ease of use and low toxicity; the ideal bath would have been thiophene/nitrogen or 3-heptanone/ $\text{CO}_2$  (both have  $T = -38\text{ }^\circ\text{C}$ , where  $\text{N}_2\text{O}_4$  has a vapor pressure of 10 Torr). Nevertheless, the dry ice/ethanol slurry allowed accurate control of the  $\text{NO}_2$  pickup pressure at the optimal value of 20–30 mTorr. It is worth mentioning that it is possible that  $\text{N}_2\text{O}_4$  forms in the droplet (it may even form in the pickup cell, and be picked up), as there should be no significant barrier to formation from 2  $\text{NO}_2$ 's, but luckily this molecule does not absorb radiation at the wavelength used in the present experiment.

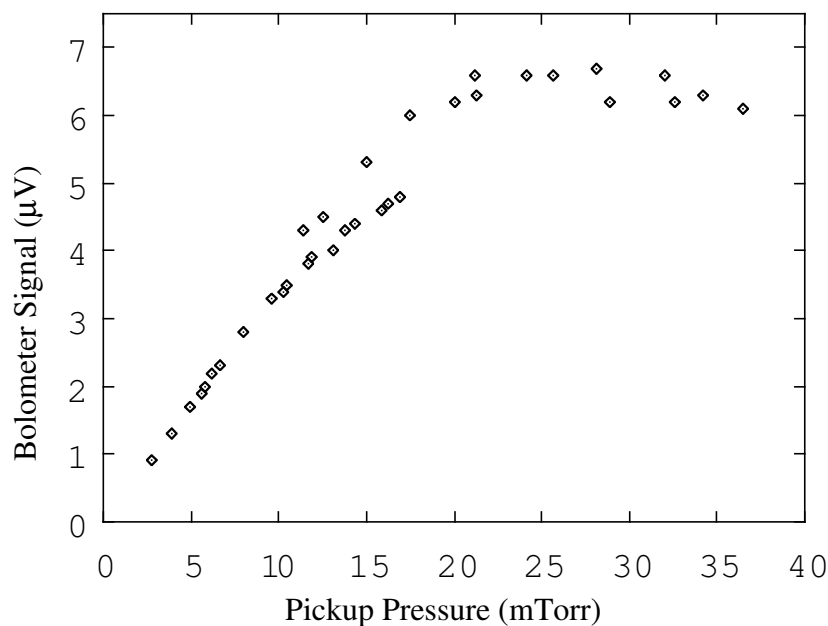


Figure 2.3: Variation of the depletion signal with an increase of the pickup pressure, at a photon energy of  $25\,400\text{ cm}^{-1}$ , and a laser power of 100 mW. Optimal performance of the pickup cell occurs at pressures ranging from 20 to 30 mTorr. Shown are the results of two runs, collected on different days. No scaling has been performed.

It is clear from these data and the estimated signal that most of the energy absorbed by the molecule is released in the droplet to evaporate helium atoms. If, above threshold, some of the energy were to be used as kinetic energy to release the photofragments out of the droplet, a sharp decrease of the bolometer signal would be observed. In fact, assuming that *all* of the energy is used to dissociate  $\text{NO}_2$  (with the excess energy released as kinetic energy of the dissociation fragments), the signal would be expected to go down near zero. The larger signal fluctuations on the low energy side of the spectrum (see Fig. 2.4) are due to a malfunction of the detector [73] which caused intense noise, and required the very long integration time (1 s pre, 100 s post time constants) for the lock-in amplifier. Even with this substantial residual noise, it is possible to conclude that no *significant* drop in signal is observed, and that a constant fraction of the photon energy is relaxed as evaporation of helium atoms. However, if a subtle effect were to be expected, the scanning of the laser would have to be improved in order to allow high resolution scans. Currently, such scans are not possible because of the poor mechanical stability of the laser's internal elements alignment (probably the vertical tilt of the tuning mirror, see Fig. 1.7) that causes the output beam to drift vertically and induce large signal excursions due to scattered light.

## 2.4 Laser Induced Fluorescence of $\text{NO}_2$

This part of the experiment turned out to be quite sparse, in terms of amount of data, but this section will show that the results are valuable in spite of our failure to detect any fluorescence signal from the embedded  $\text{NO}_2$ . First, from gas phase  $\text{NO}_2$  (unavoidable effusion from the pickup cell), it was possible to record a substantial fluorescence signal (see Fig. 2.5). Since the relaxation time of  $\text{NO}_2$  in the gas phase

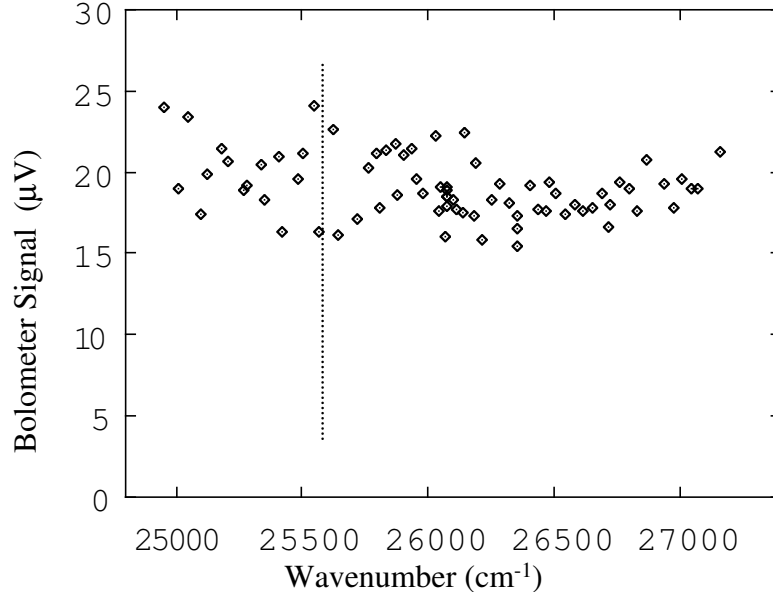


Figure 2.4: The beam depletion of NO<sub>2</sub> in the 25 000 to 27 147 cm<sup>-1</sup> (400 to 368 nm) region. The gas phase threshold (25128.57 cm<sup>-1</sup>, 398 nm) is indicated by the dashed line

(and below the threshold) is rather long, on the order of microseconds [65], it is possible to set the gated photon counter to a long delay (100 ns, in this case), thus avoiding counting scattered light photons coming from the  $\sim 10$  ns (FWHM) excitation pulse. Above the dissociation threshold, the lifetime drops by over three orders of magnitude, and no fluorescence can be observed (refer to section 2.2). From the data of Fig. 2.5, we can get a rough estimate of the dissociation threshold, although the value we get corresponds to a high temperature spectrum where rotation affects the dissociation dynamics [60]. At 0 K, no molecule has any excess energy, so each of them would dissociate *at* the threshold. When the thermal bath supplies energy to the system, it is possible to observe molecules dissociating when provided with less energy than required, since their internal energy contributes to the dissociation.

Consequently, instead of observing sharp lines, as in Ref. 65, our spectrum consists of broad resonances due to the contribution of multiple rotational states.

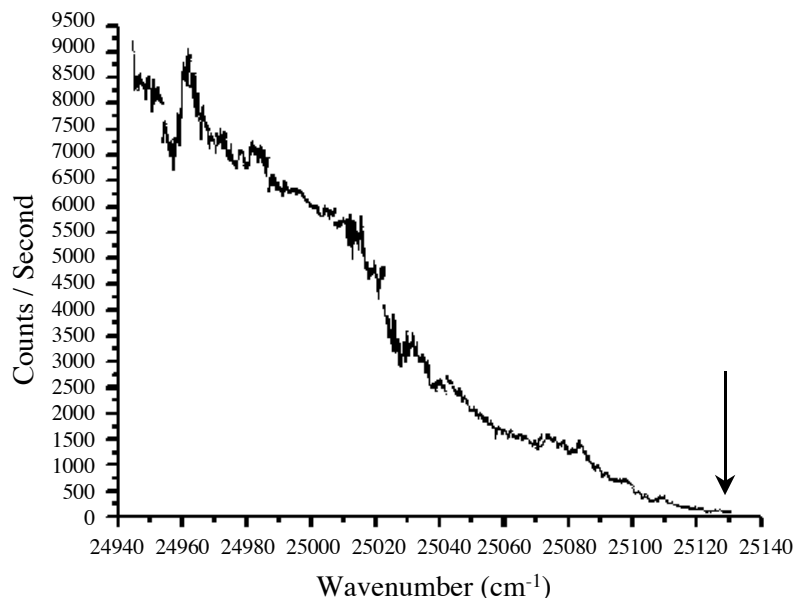


Figure 2.5: Gas phase fluorescence spectrum of NO<sub>2</sub>. The spectrum has been recorded in several pieces, on different days, and the intensity has been normalized by matching overlapping sections. No absolute frequency reference has been used; only relative frequency calibration has been performed. The dissociation threshold (25 128.57 cm<sup>-1</sup>, indicated by the arrow) cannot be determined exactly from this spectrum due to spectral dilution. Already at 25 125 cm<sup>-1</sup>, the signal gets lost in the noise, set to 10 counts/seconds.

From the molecules embedded in the droplets, no fluorescence signal has ever been observed: The laser has been scanned from 25 286 cm<sup>-1</sup> (158 cm<sup>-1</sup> to the blue of the threshold) down to 24 800 cm<sup>-1</sup> (328 cm<sup>-1</sup> to the red). Due to the expected rovibrational relaxation time of less than 20 ns [34] (electronic relaxation is even faster, see for example Ref. 36, where the decay of electronically excited K<sub>2</sub> is observed to be faster than 80 ps), only a very short, or zero delay was set on the counter. Runs with and without NO<sub>2</sub> in the pickup cell gave exactly the same

signal on the photon counter, indicating that nothing more than scattered light was collected. To minimize scattered light from the laser, a long pass filter was used. We chose to completely cut the incoming laser, and let through only 400 nm and longer wavelength (50% transmission at 435 nm, according to the manufacturer [55], measured transmittance of 0.10 at 400 nm). Since fluorescence emission is very broad in the gas phase (the excited state couples to a large number of ground vibrational states), substantial fluorescence was expected at longer wavelength than the excitation. Even with this setup no signal has been recorded, confirming that the signal recorded without the filter was exclusively laser radiation scattered from the droplet beam. Repeating the gas phase  $\text{NO}_2$  measurement with the filter in place reproduced the previously observed signal, within experimental uncertainty.

The observed depletion signal permits the calculation of the expected magnitude of the fluorescence signal which, in turn, allows the calculation of a lower limit for the rate of the relaxation mechanism that competes with fluorescence. As shown on Fig. 2.4, the depletion signal is about  $20 \mu\text{V}$ . The spectrum was taken at a nozzle temperature of 16 K, and we know that each helium atom impinging on the surface of the bolometer deposits  $5/2 kT$  of kinetic energy. The observed signal corresponds to a depletion of  $1.7 \times 10^{11}$  helium atoms per second, for 42 laser crossings. The laser wavelength is, say 400 nm ( $25\,000 \text{ cm}^{-1}$ ), and one helium atom needs  $5 \text{ cm}^{-1}$  to evaporate from the droplet. The laser is Q-switched at 1 kHz, so for each laser shot, 800  $\text{NO}_2$  molecules are excited, and relax in the droplet. From the high resolution study of Jost *et al.* [65], the gas phase emission rate below the threshold is assumed to be  $2 \times 10^5 \text{ Hz}$  (from a decay of “a few  $\mu\text{s}$ ”). This value gives a fluorescence yield of  $1.6 \times 10^8$  photons per second per laser shot. Then considering the solid angle that illuminates the fiber bundle (about 0.034, calculated from a  $15^\circ$  acceptance angle), the transmission of the fiber (about 40%, from 400 to

500 nm), and the quantum efficiency of the PMT (on average, 5% from 400 to 500 nm), we can calculate that  $1.1 \times 10^5$  photons per second per laser shot would be counted. The discriminator of the photon counter was set to measure 10 dark counts per second (cps); no signal was observed. If the predicted signal is suppressed by a relaxation mechanism that acts on a timescale  $\tau$ , such that the observed signal is, at most, equal to the noise level, then  $\tau$  may be determined by

$$1.1 \times 10^5 \frac{\text{counts}}{\text{s} \cdot \text{shot}} \times \tau \leq 10 \frac{\text{counts}}{\text{s}} \cdot \frac{1}{1000} \frac{\text{s}}{\text{shot}}$$

Consequently, the relaxation mechanism competing with fluorescence, below the gas phase threshold, must act on a timescale faster than  $\tau = 90$  ns to suppress the signal to below 10 cps. Since rotational cooling has been measured to occur within  $\sim 20$  ns following microwave excitation [19, 33, 34], it is reasonable to believe that vibronic cooling may happen on a similar timescale.

## 2.5 Determination of the Relaxation Mechanism of NO<sub>2</sub> in Helium

In order to explain the rather surprising result that NO<sub>2</sub> does *not* seem to dissociate in helium, even with an excess energy as high as 2000 cm<sup>-1</sup>(see Fig. 2.4), one has to come up with a mechanism that is consistent with the experimental data. In the previous section, the hypothesis of cooling competing with emission, thus suppressing fluorescence, explained the absence of NO<sub>2</sub> signal below the dissociation threshold. However, the relaxation mechanism above the threshold is yet to be elucidated. This section will discuss four different relaxation pathways, and their

compatibility with the experimental data.

- 1– The molecule doesn't dissociate at all because vibrational relaxation in the ground state is faster than dissociation: it is brought to the  $\tilde{A}^2B_2$  state, crosses back to the ground  $\tilde{X}^2A_1$  state, and immediately cools instead of dissociating.
- 2– The molecule dissociates, but there is not enough excess energy to escape the confining potential of the droplet, and the fragments recombine. This scenario leads to three distinct possibilities:
  - a) The fragments recombine in the exact same electronic state as the original doublet state, and all the photon's energy is released as the NO—O chemical bond is formed.
  - b) As in case a), the fragments recombine, but a (possible) barrier to bond formation cannot be overcome at the low temperature of the droplet, and a van der Waals complex NO···O is formed.
  - c) While the fragments are far apart, some spin shuffling occurs (due to spin-orbit coupling in the fragments) and the final electronic state is a mixture of the original doublet state ( $\tilde{A}^2B_2$ ), and a new state of different spin degeneracy (a quartet:  $1^4A_1$ ).

The first mechanism simply states that as the molecule absorbs energy from the electromagnetic field, it is immediately relaxed into the bath and evaporates helium atoms, *as the molecule extends towards dissociation*. So far, this is the most likely mechanism, as it is fully compatible with both the beam depletion, and the fluorescence collection experiments. The first version of the second mechanism (2a), apart from the excursion of the fragments to the bulk of the droplet,

before reassociating, corresponds to mechanism 1. It is somewhat different because photodissociation *does* occur, but the current experimental setup only sees the *final* state of the system, and does not permit the observation of the difference in terms of “pathways”. If this mechanism could be established, it would indicate that no “long-range” barrier to recombination exists for NO + O. The next section (2.6) will present a modification to the experiment which would permit the observation of transient photodissociation products, if they form. The third possibility (2b) is not compatible with the beam depletion data. If the fragments were to form a van der Waals complex, then some energy would be “kept” in the complex. This kind of complex is not as low in energy as a molecule formed of the same components, as the dispersion forces holding together the fragments are not as strong as a chemical bond. If such complex formed, and did not decay, then the beam depletion data would show a decrease in the signal, as less helium atoms would be evaporated upon complexation. As for the fourth possibility, scenario 2c, the final distribution of electronic states would be entirely statistical, and governed by the electronic configuration degeneracy. Instead of having all the molecules in the  $\tilde{A}^2B_2$  state, only one third of them would recombine and then cool through the ground state, while the remaining 2/3 would be trapped in the  $1^4A_1$  excited state, forced to decay *via* fluorescence, but unable to do so because it is a spin-forbidden process. However, intersystem crossing dynamics could be enhanced by the helium environment, and rapid conversion of the  $1^4A_1$  state to the  $\tilde{A}^2B_2$  or the  $\tilde{X}^2A_1$  states could occur. This relaxation scheme could be compatible with the beam depletion experiment, if and only if the intersystem crossing is faster than the time-of-flight of the droplets from the laser crossing to the bolometer. If some population is truly trapped in the  $1^4A_1$  state for a long time, then this mechanism becomes equivalent to 2b (with different electronic states involved), thus not compatible with the experimental data.

In order to elucidate the relaxation mechanism, it is imperative to determine whether or not dissociation products form, following the electronic excitation of NO<sub>2</sub> to the  $\tilde{A}^2B_2$  state. The last section of this chapter will present the details of an experiment devised to detect the formation NO.

## 2.6 Outlook: Laser Induced Fluorescence of NO. Towards the Detection of Transient Photodissociation Products

It has been suggested in the previous section (2.5) that embedded NO<sub>2</sub> may dissociate upon excitation, and then rapidly recombine before cooling. Unfortunately, this scenario is impossible to distinguish from the case where NO<sub>2</sub> relaxes quickly and never dissociates, as both pathways lead to the same long-time limit: the relaxation of *all* the photon's energy into the droplet, and evaporation of helium atoms (monitored in a beam depletion experiment). The absence of fluorescence from the embedded species suggests a cooling mechanism faster than about 90 ns. This "fast relaxation" requirement does not exclude the possibility that the dissociation fragments, NO and O, extend far enough from each other to allow NO to be probed as an isolated species. The detection of NO has become a very efficient procedure to elucidate combustion chemistry mechanisms, and to study environmental pollution. Several extremely sensitive techniques have been developed, including laser induced fluorescence. This section will outline the implementation of a two-photon NO detection scheme into our HENDI NO<sub>2</sub> experiment.

The electronic spectroscopy of NO is well understood, and the  $A^2\Sigma^+ \leftarrow$

$X\ ^2\Pi$  transition (the gamma band) has been studied for many years. Both its single-photon and two-photon cross sections have been determined accurately, and most of its vibronic structure has been assigned. The band origin of the  $A\ ^2\Sigma^+ - X\ ^2\Pi$  manifold is located at 226 nm, well outside the range of the Indigo (when quadrupled, its output can access the range 207–184 nm). Fortunately, the vibrational structure of the  $A\ ^2\Sigma^+$  state could allow us to probe the (2,0), (3,0), and (4,0) lines, with wavelengths of 204.9, 195.8, and 187.6 nm [74], respectively. The standard notation is used:  $(v', v'')$ , with  $v'$  the excited state's vibrational quantum number, and  $v''$  the ground state's. Note that at the temperature of the helium droplet, 0.38 K, the ground state is completely vibrationally relaxed, and all transitions must originate from  $v' = 0$ . Three different schemes can be used to generate light at these wavelengths (*i.e.* to quadruple the Indigo): one can either install Positive Light's quadrupler setup, which would require a complete reorganization of the laser, or one can try to externally double the doubled output of the laser. A third possibility does not require quadrupling the laser's output, but hitting a two-photon transition to the excited state in the blue (the doubler's output, around 400 nm). The two-photon alternative, will be outlined first, as it does not involve any change to the laser setup. The method relying on externally doubling the doubled output of the Indigo will close this section. The use of the quadrupler will not be discussed, as it is fundamentally equivalent to the external doubling of the blue output, but inconvenient due to the present use of the laser.

### 2.6.1 Two-Photon $A - X$ Transition

Burris, McGee and McIlrath [75] have studied the two-photon process in the gamma band of NO, using four wave mixing technique. They reported an accurate determi-

nation of its cross section:  $\sigma^{(2)} = (2.9 \pm 1.8) \times 10^{-49} \text{ cm}^4 \cdot \text{s}$ . It compares favorably with the value reported by Hochstrasser [76],  $\sigma^{(2)} = 2.9 \times 10^{-49} \text{ cm}^4 \cdot \text{s}$  (without error bars, also measured *via* four wave mixing technique). The main advantage of the two-photon technique lies in the ease of measuring fluorescence without worrying about laser scattering: the excitation wavelength is about 200 nm away from the collection wavelength. Using the appropriate optical filter, one can collect fast fluorescence (the gas phase lifetime of electronically excited NO has been measured to be on the order of 200 ns for the  $A \ ^2\Sigma^+$ ,  $v' = 0$  state [74]) with good signal-to-noise. Unfortunately, the absorption cross section is rather low, and to efficiently pump this transition, one needs lots of laser power. The Evolution X/Indigo laser system, when doubled, provides 200 mW of power at a repetition rate of 1 kHz; this corresponds to 200  $\mu\text{J}$  per pulse (see Sec. 1.2.2). At 400 nm, with a photon energy of  $5 \times 10^{-19} \text{ J}$ , this value yields a flux of  $4 \times 10^{14}$  photons/pulse. For 10 ns pulses, the photon peak flux is  $4 \times 10^{22}$  photons/(s-pulse). With the laser focused to a 50  $\mu\text{m}$  spot size, we obtain a peak fluence of  $8 \times 10^{26}$  photons/(s-pulse $\cdot\text{cm}^2$ ). The probability of excitation, for a two-photon process can be calculated from the two-photon cross-section  $\sigma^{(2)}$ , the fluence  $f$ , and the pulse duration  $\Delta t$ :

$$P = \sigma^{(2)} \times f^2 \times \Delta t \tag{2.1}$$

From the values given above, we get that  $P = 1.9 \times 10^{-3}$ , so 0.2% of the molecules would be excited at each laser pulse.

In a beam of droplets that generates 8.1 mV of signal (as described in sections 1.1.2 and 2.3), we have the equivalent of  $4.6 \times 10^9$  droplets of  $\sim 15\ 000$  atoms hitting the bolometer, per second. Under optimal conditions,  $1/e$  of these will be doped after crossing the pickup cell, thus we consider a flux of  $1.68 \times 10^9$

NO molecules going through the laser spot per second. At that point, the droplet beam is about 1 mm in diameter (for an area of  $7.9 \times 10^{-7} \text{ m}^2$ ), and it travels at 450 m/s, so the density of molecules crossing the laser is

$$\frac{1.7 \times 10^9 \text{ NO/s}}{7.9 \times 10^{-7} \text{ m}^2 \cdot 450 \text{ m/s}} = 4860 \text{ NO/mm}^3 \quad (2.2)$$

The laser is focused to a spot size of 50  $\mu\text{m}$  (for a waist of 25  $\mu\text{m}$ ). For a length corresponding to the droplet beam diameter (1 mm), the excitation volume is  $2 \times 10^{-3} \text{ mm}^3$ . Consequently,  $4860 \text{ NO/mm}^3 \times 2 \times 10^{-3} \text{ mm}^3 = 10 \text{ NO molecules}$  would be irradiated, at each laser shot. If 0.2% of them are *excited*, and the repetition rate of the laser is 1000 per second, we'd expect to excite 20 NO molecules per second. Assuming that the fluorescence quantum yield is 1.0 (which is a good estimate for a molecule like NO), we could collect about 20 photons/s. In the present case, since we are not using the fiber bundle, the collection efficiency is much better: the acceptance angle of the PMT can be as large as 30° (the bundle's is about 15°), and no losses occur as would in the bundle. Globally, we estimate that 14% of the photons will arrive at the PMT (compared to 1.3% with the bundle). With a quantum efficiency of 10%, the output of the detector would read about 0.3 cps, which translates to a signal-to-noise ratio of 0.03 when setting the photon counter discriminator to read a dark count of 10 cps. This experiment is not expected to work. The failure can be attributed to the vanishingly small excitation volume induced by the tight focusing needed to increase the peak photon flux to compensate for the small absorption cross section. Furthermore, since the predicted NO population would be much smaller in the NO<sub>2</sub> experiment, where we excite at most 1% of all the NO<sub>2</sub> molecules in the beam, the two-photon detection scheme is definitely bound to fail.

## 2.6.2 One-Photon $A - X$ Transition

Following the procedure of the previous section, the prediction of the signal for the single-photon excitation can easily be calculated. The cross section for the  $A \ ^2\Sigma^+$  to  $X \ ^2\Pi$  transition is known [74] to be  $5 \times 10^{-19} \text{ cm}^2$ . From the  $\text{NO}_2$  experiment, it has been shown that the output of the Indigo can be maintained well over 200 mW in the ultraviolet, around 400 nm. Single-pass external doubling with a LBO crystal similar to the one used inside the laser box could be performed, and an efficiency of about 10% can be expected, so the laser power in the 200 nm region would be 20 mW (or 20  $\mu\text{J}$  per pulse). From the previous section, the NO density in the beam at the laser crossing point is 4860 NO/mm<sup>3</sup>. The laser can be focused to a 500  $\mu\text{m}$  spot size, over the droplet beam diameter, for an excitation volume of 0.2 mm<sup>3</sup>. Thus, about 970 NO molecules would be illuminated per laser shot. The laser fluence, from 200 nm photons at 20  $\mu\text{J}$ /pulse for 10 ns pulses, with the spot size given above, is  $f=1 \times 10^{24} \text{ photons}/(\text{s}\cdot\text{cm}^2)$ . Using equation 2.1, we find that 0.5 % of the molecules would be excited under these conditions. With the density calculated above, we predict that 5 NO molecules would be excited per laser shot, and at a repetition rate of 1 kHz, 5000 NO molecules would be excited per second. Assuming (again) a quantum yield of 1.0 for NO and that 14% of the photons arrive at the PMT (which has a 10% quantum efficiency), we can predict a signal of 70 cps, for a signal-to-noise ratio of 7 with the dark counts set to 10 cps. The excitation rate can be optimized by varying the focal spot of the laser with different lenses, but this calculation shows that detection of NO using external doubling of the ultraviolet output of the Indigo is possible, and should be attempted.

## Chapter 3

# Experimental Observation of the Breakdown of the Adiabatic Following Approximation <sup>1</sup>

As discussed in the introduction, the extra moment of inertia added by the helium for fast rotors is “anomalously” small, *i.e.* the superfluid density does not succeed in following the rotation fast enough, and a breakdown of adiabatic following occurs. The topic of adiabatic following applied to the rotation of impurities in superfluid helium has been described thoroughly by several groups and the limitations of the model are now well understood [6, 21]. Unfortunately, these limitations are rather difficult to probe experimentally, since the behavior of molecules in helium is a mixture of rotational and vibrational effects. Microwave spectroscopy allows the study of the relaxation of rotors without the contribution of vibrational effects. Furthermore, the ability to probe isotopically substituted species allows, to a certain extent, the interaction potential between the host and the matrix to be kept constant. This chapter will report on the observation of pure rotational spectra of isotopically sub-

---

<sup>1</sup>The material related to the HCN/DCN experiment has been published in A. Conjusteau *et al.*, *J. Chem. Phys.*, 113:4840, 2000

stituted species. Firstly, the rotational (microwave) spectrum of HCN and DCN embedded in  $^4\text{He}$  nanodroplets has been measured. The  $J = 0 \rightarrow 1$  transitions for both molecules have been recorded at 72.21 and 59.90 GHz respectively. Power-saturation measurement have also been performed, and show that the rotational relaxation time for these molecules is on the order of  $10^{-8}$  s. Secondly, a similar experiment has been performed with  $\text{CH}_3\text{F}$  and  $\text{CD}_3\text{F}$ , and the pure rotational spectra of both species has been observed: the resonances are found at 43.2 and 36.1 GHz, respectively. The increase in moment of inertia due to the presence of liquid helium, which the assumption of adiabatic following of the helium density predicts should be almost identical for each member of both HCN/DCN and  $\text{CH}_3\text{F}/\text{CD}_3\text{F}$  pairs. In the case of the cyanides, the increase is found to be 9% smaller for the faster of the two rotors, HCN. This result is interpreted as a breakdown of the adiabatic following approximation. It is impossible at present to assign with certainty the transitions observed for the  $\text{CH}_3\text{F}/\text{CD}_3\text{F}$  system, but preliminary analysis shows that the spectra are consistent with the assumptions of the adiabatic following model.

### 3.1 Introduction

HENDI spectroscopy provides a way to study the finite-size properties of superfluid helium [17], as well as a way to form and study novel metastable chemical species [24, 25] (see also Chap. 2). An unusual feature of rovibrational spectra in this condensed medium is the extremely slow ( $< 10^9 \text{ s}^{-1}$ ) rate of rotational dephasing [33], which allows even heavy and/or highly anisotropic molecules, such as OCS [17],  $\text{SF}_6$  [14, 77], HCCCN [34],  $(\text{HCN})_2$  [78], and even  $(\text{CH}_3)_3\text{SiCCH}$  [20] to display resolved rovibrational transitions with the same spectral structure as dictated by the symmetry of the isolated molecule. Such rotationally resolved spec-

tra have allowed the determination of the rotational temperature of the solute (0.38 K [77]), which is found to be largely independent of cluster size and is in agreement with previous predictions of the droplet temperature based on evaporative cooling [15, 16]. The moments of inertia of a molecule that rotates in superfluid  $^4\text{He}$  have been found, however, to be up to five times larger than those of the isolated molecule [6, 14, 17, 20, 34, 77].

The ability to reliably calculate the rotational constants of molecules solvated in liquid helium would provide insight into the interactions between the molecule and the quantum liquid that surrounds it, and into the dynamics of atomic motion in the helium. Furthermore, such a theory would improve our ability to use rotationally resolved HENDI data to obtain structural information. At present, two models have been put forward to explain the observed increase in the moment of inertia. The first is based on the idea that a fraction of the atoms in the first He solvation shell is subtracted from the superfluid and rotates rigidly with the molecule, leading to an increased moment of inertia. With judicious choice of the “normal fluid” fraction, this model has been able to explain the observed increase in the moment of inertia of  $\text{SF}_6$  and  $\text{OCS}$  [14, 17]. The rather *ad hoc* nature of this definition of “normal fluid” density has recently been addressed by Kwon and Whaley [79] who have proposed a computational definition of a spatially dependent “normal fluid” density which is evaluated by finite temperature Path Integral Monte Carlo (PIMC) calculations. These authors have reported that they can predict the rotational constant of  $\text{SF}_6$  to within the experimentally determined accuracy of  $\approx 1\%$ .

The second model is based on the notion that rotation of a rigid body in superfluid helium produces fluid displacement, which leads to an increased in-

ertia. Such a hydrodynamic contribution to the effective moment of inertia of a molecule solvated in an ideal liquid of uniform density (equal to that of bulk liquid He) had been considered earlier, but was found to be a minor fraction of the experimental value [4, 17, 22]. Recently, however, we have performed hydrodynamic calculations that properly account for the anisotropy of the He density around the solute molecule [6]. Accordingly, the increase in the rotational inertia has been found to be sufficient for the quantitative prediction of the observed effective moments of inertia for several molecules. An important assumption of the hydrodynamic model is that while the helium flow remains irrotational, the fluid’s *density* adiabatically follows the rotation of the molecule, much like a wave. Thus, both existing models include adiabatic following of the molecular rotation by the surrounding helium, although under two quite distinct forms. Recent fixed-frame Diffusion Monte Carlo (DMC) calculations for SF<sub>6</sub> have found, however, that the helium density does not perfectly follow the molecular rotation [5]. When the static rotational constant of the free SF<sub>6</sub> molecule was artificially increased by a factor of 10, greatly increasing the rotational speed, the modulation of the helium density in the rotating molecular frame as well as the corresponding solvation-induced increase in the moment of inertia were substantially reduced.

Experimentally, it has been found that rotors with large rotational constants (i.e. fast rotational speeds), such as H<sub>2</sub>O, NH<sub>3</sub> [80, 81] experience, at most, a modest increase of their moments of inertia upon solvation in He. However, the interaction potential of such molecules with He is also more isotropic than for molecules such as SF<sub>6</sub> and OCS, which, independently, leads to smaller solvation-induced changes in the moment of inertia. Therefore, from these observations alone, it is not possible to assess quantitatively any deviation from the adiabatic following hypothesis. To address this problem, we decided to perform pure microwave spectroscopy

experiments of isotopically substituted systems: HCN/DCN, and CH<sub>3</sub>F/CD<sub>3</sub>F.

In the case of HCN, the rotational constant of the embedded species is already known to be 35.23 GHz, from an infrared Stark experiment reported by the group of Miller [82]. The increase in moment of inertia induced by the helium can be calculated. Assuming that a similar effect is felt by DCN, we can predict the position of the  $J=0 \rightarrow 1$  resonance to be near 66 GHz (from 72.2 GHz). These results are presented in section 3.2. In the case of CH<sub>3</sub>F and CD<sub>3</sub>F, the situation is different. These molecules have never been observed in helium, so their effective (solvent altered) rotational constants are not known. The gas phase rotational constant of both molecules places them in an intermediate range of rotational velocity, between the truly fast rotors (like HCN, H<sub>2</sub>O, NH<sub>3</sub>) and the slow ones (like (CH<sub>3</sub>)<sub>3</sub>SiCCH), so it is very hard to predict how far the resonance of the embedded species will be shifted:  $B$  can be reduced by as little as 2% [83], or as much as 500% [20]. It is known that fast rotors are weakly affected by helium, whereas slow ones see their rotational constants reduced by a factor of 3 to 5 [20]. These issues will be addressed in section 3.3.2.

The magnitude of the solvent-induced increase in moment of inertia for the isotopically substituted molecules, in each pair is expected to be almost identical, under perfect adiabatic following conditions; they experience the same interaction with He. Any difference, yielding a smaller increase for the faster of the two rotors, can be attributed to a breakdown of the adiabatic following approximation. Since the isotope substitution shifts the center of rotation for the two molecules, a hydrodynamic correction is also present. This correction is, however, opposite in sign to the main effect.

## 3.2 Microwave Spectroscopy of HCN and DCN

Figure 3.1 shows the MW spectra measured for HCN and DCN. The top panel is the HCN resonance, roughly centered on 72.1 GHz. The bottom panel shows the DCN resonance around 59.8 GHz. The arrow on the top panel shows the position where the HCN resonance would be expected if the increase of moment of inertia of HCN were the same as that of DCN. In both panels, the position of the main peak (\*) and of the center of mass (CM) of the spectral feature are identified; the first quantity is taken as the definition of the transition frequency used to calculate the rotational constants

These molecules have sufficiently large rotational constants that only the  $J = 0$  rotational state is significantly populated at the temperature of the droplets (0.38 K), thus the observed line is assigned to the R(0) transition (furthermore, the HCN rotational constant is already known, see above). For both spectra, +9.3 dBm ( $\approx 8.5$  mW) of microwave radiation were used. This value corresponds to the highest available power that remained leveled through the entire spectrum, and was chosen to maximize the signal amplitude; the corresponding intensity at the center of the waveguide is  $107$  mW/cm<sup>2</sup>. Saturation measurements (see Figure 3.2) were performed to ensure that the spectra were not power broadened. The data show that at this power level both transitions are fully saturated. No position- or lineshape-dependence has been observed using lower MW power, down to +3.0 dBm ( $\approx 2$  mW), thus confirming that the observed line broadening is mostly inhomogeneous and that power broadening is not significant, even at the highest power used.

From the saturation data of Fig. 3.2, under some simplifying assumptions, it is possible to estimate the saturation intensity  $I_s$ , hence the product  $T_1 T_2$  of

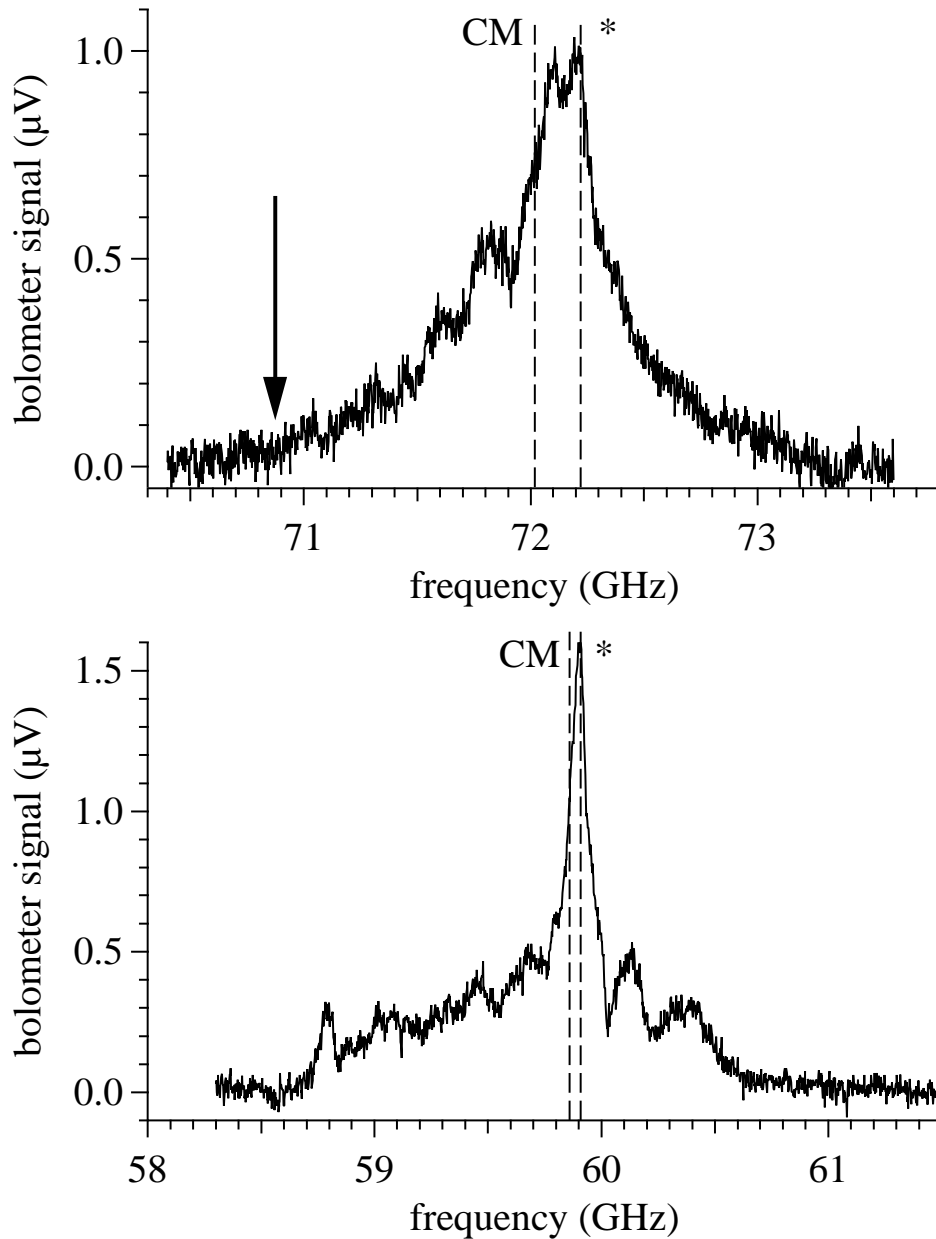


Figure 3.1: Top panel: HCN rotational spectrum, R(0) line. The arrow shows the expected position of the HCN resonance, if its increase of moment of inertia were the same as that of DCN. Bottom panel: DCN rotational spectrum, R(0) line. On both panels, the position of the main peak (\*) and of the center of mass (CM) of the spectral feature are identified.

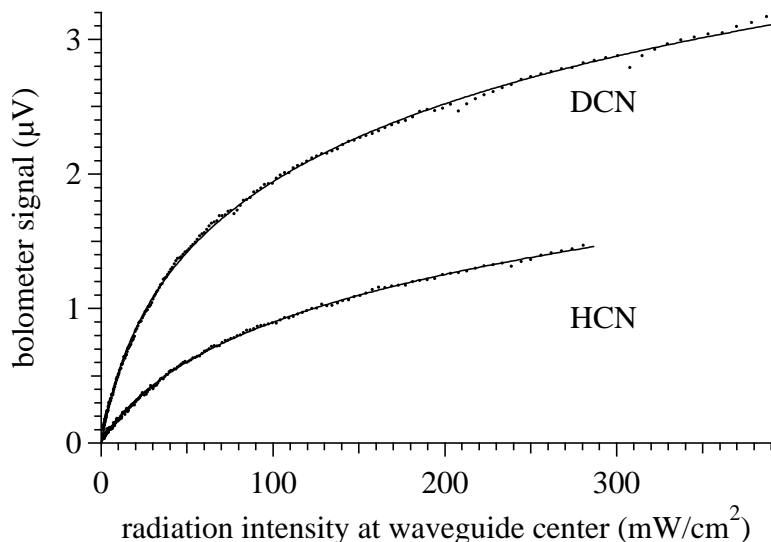


Figure 3.2: Saturation behavior of the HCN and DCN transitions. In each case, the signal near the maximum (HCN: 72.222 GHz, DCN: 59.904 GHz) is displayed against the microwave intensity at the center of the waveguide. The solid lines are the fitting curves associated with the parameters of Tab. 3.1.

the population- and transverse-relaxation times [84]. In the present context, the meaning of  $T_1$  and  $T_2$  is similar to that of NMR spectroscopy, as these variables represent the timescales of, respectively, the population decay from the excited state to the ground state, and rotational dephasing (how a body’s rotation is “interrupted” by a collision, without leading to relaxation to the ground state). We assume that all molecules are irradiated with the same intensity, taken to be that at the center of the waveguide. The observed line is supposed to be the convolution of a *static* inhomogeneous distribution with a homogeneous (Lorentzian) line; in the case of DCN, only the sharp most intense line is considered. It is empirically found that among simple analytical functions, the one that best describes both the HCN and

DCN inhomogeneous profile has the form:

$$\begin{cases} \exp(\Delta\nu/w_-) & \text{if } \Delta\nu < 0 \\ \exp(-\Delta\nu/w_+) & \text{if } \Delta\nu \geq 0 \end{cases} \quad (3.1)$$

$\Delta\nu$  being the detuning from the position of the maximum,  $\nu_0$ ; the best fit values of  $\nu_0, w_-, w_+$  are reported in Table 3.1. We then fit the data in Fig. 3.2 to the intensity at zero detuning as a function of microwave intensity; the best fit values of  $I_s$  and  $T_1T_2$  are also reported in Table 3.1. We remark that, under the above assumptions, the value of  $T_1T_2$  does not strongly depend on the functional form chosen, as long as the latter reasonably describes the observed inhomogeneous profile. Assuming static inhomogeneous broadening, a lower limit on  $T_2$  is set by the full width at half maximum  $w$  of the observed peak:  $T_2 \geq (\pi w \sqrt{1 + I/I_s})^{-1}$ , with  $I = 0.107 \text{ W/cm}^2$ ; we have then  $T_2 \geq 1.2 \text{ ns}$  for HCN and  $T_2 \geq 8 \text{ ns}$  for DCN. More likely,  $T_1$  and  $T_2$  are of comparable magnitude, *i. e.*  $\approx 12 \text{ ns}$  for HCN and  $\approx 17 \text{ ns}$  for DCN. These values are comparable to those previously measured for cyanoacetylene [33].

	$\nu_0$ (GHz)	$w_-$ (GHz)	$w_+$ (GHz)	$I_s$ (mW/cm <sup>2</sup> )	$T_1T_2$ (ns <sup>2</sup> )
HCN	72.17	0.45	0.25	30	150
DCN	59.90	0.098	0.075	14	300

Table 3.1: Best fit parameters for the lineshapes of Fig. 3.1 and the saturation data of Fig. 3.2.

If higher order terms (the leading one being centrifugal distortion) are ignored, the rotational constants are simply one half of the R(0) transition frequency. The value of the resonance frequency constants cannot be exactly defined from the experimental spectra, since one could arbitrarily use the position of the maximum

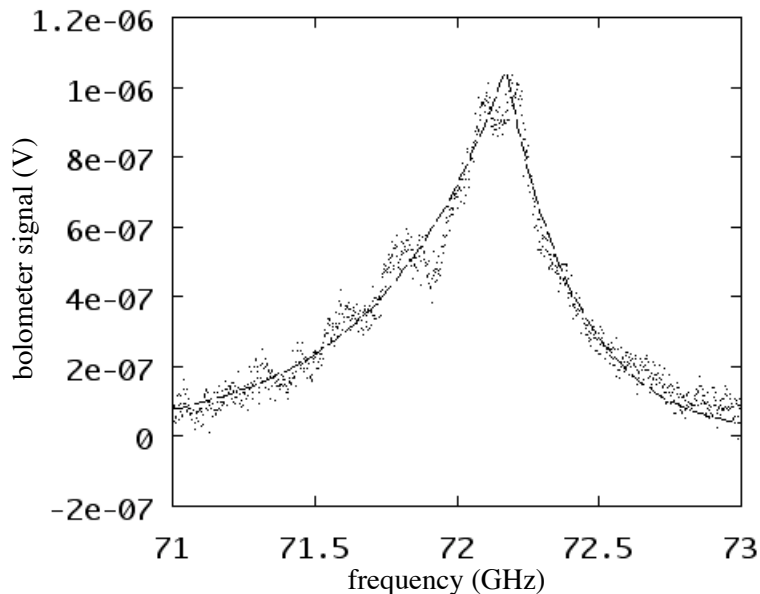


Figure 3.3: Fit of the HCN resonance showing the results of table 3.1. The spectral data from Fig. 3.1 (top panel) is reproduced as small dots for clarity. The fit is shown as a dashed line.

or that of the center of mass. We decided to use the former quantity (see Fig. 3.1), and to use the difference between the two as an estimate of the uncertainty. For HCN the maximum at 72.21 GHz is used; the center of mass is calculated to be at 72.02 GHz. For DCN the maximum is located at 59.90 GHz and the center of mass (with the calculation restricted to the 58.6–60.7 GHz range) is found to be at 59.86 GHz. With these values, rotational constants of 36.11(10) and 29.95(2) GHz are determined for HCN and DCN respectively.

The rotational constant for the  $v(\text{CH}) = 1$  vibrational state of HCN in He nanodroplets was previously determined, using Stark spectroscopy, to be  $1.175 \text{ cm}^{-1}$  (35.23 GHz) by Nauta and Miller [82]. Ours is the first determination of the rotational constant of HCN in its ground state. One can see that vibrational effects are

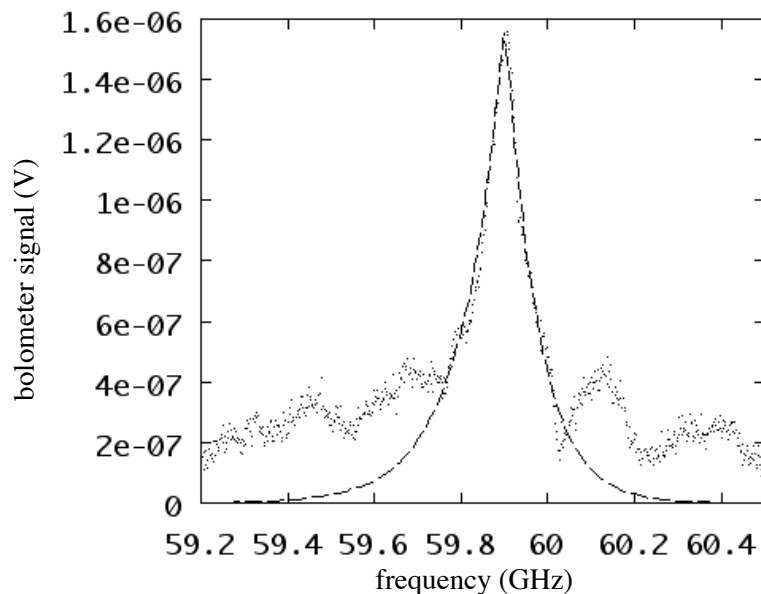


Figure 3.4: Fit of the DCN resonance showing the results of table 3.1. The spectral data from Fig. 3.1 (bottom panel) is reproduced as small dots for clarity. The fit is shown as a dashed line. Note that the frequency scale is different from that of Fig. 3.3, as the main spectral feature is much narrower.

small but not negligible ( $\Delta B=0.88$  GHz). In Table 3.2 we report the observed moments of inertia for both HCN and DCN, in gas phase and in  $^4\text{He}$  droplets and their differences. Also given in Table 3.2 is the increase in moment of inertia predicted by the superfluid hydrodynamic model [6] if perfect adiabatic following is assumed. The predicted increase is negligibly smaller for DCN than for HCN because in the latter molecule, the center of mass and the geometric center are closer together, hence in a sense DCN is, dynamically, more spherical. This effect is small and more importantly, its contribution is opposite in sign to the experimentally observed trend in which the increase in moment of inertia induced by the liquid is 9% smaller for HCN than DCN.

	$I_m$	$I_{\text{eff}}$	$I_{\text{eff}} - I_m$	$I_h$
HCN	11.39	14.00	2.61	5.7
DCN	14.00	16.87	2.87	5.6

Table 3.2: Moments of inertia of HCN and DCN as free molecules ( $I_m$ ) or solvated in  $^4\text{He}$  ( $I_{\text{eff}}$ ). Their difference is to be compared to the increase ( $I_h$ ) in moment of inertia predicted by the superfluid hydrodynamic model [6] in the assumption of perfect adiabatic following. The small variation in  $I_h$  for the two isotopomers is due to the different position of their centers of mass (see text). Units are  $\text{amu}\cdot\text{\AA}^2$ .

We interpret the present results as unequivocal experimental evidence for the breakdown of the adiabatic following models (regardless of whether the “normal fluid fraction” or “pure superfluid” picture applies) in fast rotors. A 23% increase of the rotational speed (comparing gas phase HCN to gas phase DCN) results in a 9% decrease in the solvent-induced component of the moment of inertia. In order to evaluate the qualitative significance of the present results, we need a theory able to quantify the degree of adiabatic following as a function of the rotational period of the rotor. Diffusion Monte Carlo calculations could likely provide this information in the near future, considering the promising results already obtained for  $\text{SF}_6$  [5] and an excellent He-HCN interaction potential [85].

In closing this section, it is worth pointing out that qualitatively different lineshapes have been observed for the HCN and DCN transitions. The HCN R(0) line is similar to that previously observed for the R(0) transition of the  $2\nu(\text{CH})$  overtone in the same molecule [20], while the DCN transition looks more similar to that reported for the R(0) transition of the  $\nu(\text{CH})$  fundamental in HCN [82]. A thorough analysis of two sources of line broadening in He nanodroplet spectroscopy was recently published [4], in which the  $J = 0 \rightarrow 1$  transition was simulated. The predicted HCN R(0) lineshape was too narrow, unless the effect of one source of broadening (a hydrodynamic coupling of translation and rotation) was made about

6 times larger than the *a priori* estimate [20]. The shape of the DCN R(0) line measured here is instead in good agreement with the predictions of Ref. 4, with no need to scale the interaction parameters. However, the model of Ref. 4 does not contain any physical mechanism by which the remarkable difference between the two isotopomers can be justified. The qualitative difference between the lineshapes observed here was unexpected and is as yet unexplained. Recent work by Erik Draeger (Urbana–Champaign), has focused on the study and modeling of thermal excitations occurring in the first solvation layer around impurities embedded in superfluid helium nanodroplets [86]. However, a signature that the existence of localized excitations leads to this complex spectral structure has yet to be observed.

### 3.3 Microwave Spectroscopy of CH<sub>3</sub>F and CD<sub>3</sub>F

This section presents the second part of the investigation of pure rotational spectra of isotopically substituted species. A short section on the spectroscopy of prolate symmetric top will open this section, and then the experimental data will be presented, and discussed.

#### 3.3.1 The Spectroscopy of Symmetric Tops

Nonlinear polyatomic molecules have three axes of rotation: There are three distinct moments of inertia (one parallel to the principal axis, and two perpendicular to it), leading to three rotational constants,  $A$ ,  $B$ , and  $C$  (with the convention being  $A > B > C$ ). Such molecules are called asymmetric tops. When the symmetry of a molecule is such that two axes are equivalent (*i.e.* two moments of inertia are equal),

the molecule is then classified as a symmetric top. Symmetric tops can be further classified into two categories: oblate ( $B = A$ ), and prolate ( $B = C$ ).  $\text{CH}_3\text{F}$  and  $\text{CD}_3\text{F}$  are both prolate tops, and the energy of their rotational levels is expressed by the following relation

$$E(J, K) = BJ(J + 1) + (A - B)K^2 \quad (3.2)$$

where  $J$  is the rotational quantum number, and  $K$  is the component (projection) of  $J$  onto the principal axis, which can take values  $-J, \dots, 0, \dots, +J$ . Do not confuse  $K$  with  $M_J$ , the projection of  $J$  onto the laboratory frame of reference ( $M_J$  has the same selection rules as  $J$ ). Higher order terms are sometimes presented, the leading one being  $-DJ^2(J + 1)^2$ , but they will not be discussed here (see Ref. 21 for a discussion of the effect of the helium environment on  $D$ ). The selection rules for a pure-rotation are

$$\Delta J = 0, \pm 1, \quad \Delta K = 0 \quad (3.3)$$

$K$  is not allowed to change, as a symmetric top has no permanent dipole moment perpendicular to the principal axis, thus the electromagnetic (microwave, in this case) field has no “handle” to affect the rotation of the molecule in that direction.

For  $\text{CH}_3\text{F}$  and  $\text{CD}_3\text{F}$ , the rotational constant  $A$  has a gas phase value of 152.7932, and 76.85839 GHz (respectively) [87], and the current setup does not allow the observation of rotational transitions along that axis (the axis of symmetry, *i.e.* the C–F bond). The observed transitions presented in the next section correspond to an “end-on” rotation of the molecule, involving the displacement of the (heavy) F atom, thus the much larger moment of inertia (smaller rotational constant). For  $\text{CH}_3\text{F}$ , the gas phase rotational constant  $B$  has been determined to be 25.53059 GHz, whereas for  $\text{CD}_3\text{F}$ ,  $B = 20.44557$  GHz.

### 3.3.2 Microwave Spectra of CH<sub>3</sub>F and CD<sub>3</sub>F

We decided to study CH<sub>3</sub>F and CD<sub>3</sub>F because their gas phase rotational constants place them in a zone of rotational velocity that had not been sampled before, between the fast rotors like HCN (see previous section), and the slow rotors like the substituted acetylenes our group has extensively studied in the infrared [20] (recall that in the gas phase, for HCN  $B = 44.37$  GHz, and for most of the “slow” rotors studied previously,  $B \sim 5$  GHz).

The disadvantage of this system is that the permanent dipole moment of the methylfluoride isotopomers ( $\mu = 1.85$  D) is lower than those of HCN and DCN ( $\mu = 2.98$  D). Since the transition strength, in the microwave, depends upon the square of the permanent dipole moment, the largest signal we can expect from these species is about a factor of three ( $2.98^2/1.85^2 = 2.6$ ) lower than what we observed previously for HCN and DCN (assuming that the signal observed in both cases is limited by the number of absorption–evaporation cycles, see Sec. 1.3.3, and that the saturation behavior of the methyl–like species is similar to that of the cyanides). Furthermore, due to the independent cooling of the room temperature spin state populations upon solvation in helium, the rotational degrees of freedom will not completely relax, and both the  $K=0$  and  $K=1$  quantum states will remain populated, in equal proportions: The spin population being probed in this experiment clearly violates Boltzmann statistics. Since microwave spectroscopy allows us to only excite the population of *one* rotational state at a time (either the  $J=0$  or the  $J=1$ , since they resonate at different frequencies), a loss of 50% in signal amplitude will result when compared to the case of both HCN and DCN, where all the rotational population was found in the  $J=0$  state. And lastly, since the photon energy is expected to be about a half to two–thirds that of HCN, further loss in sensitivity is expected,

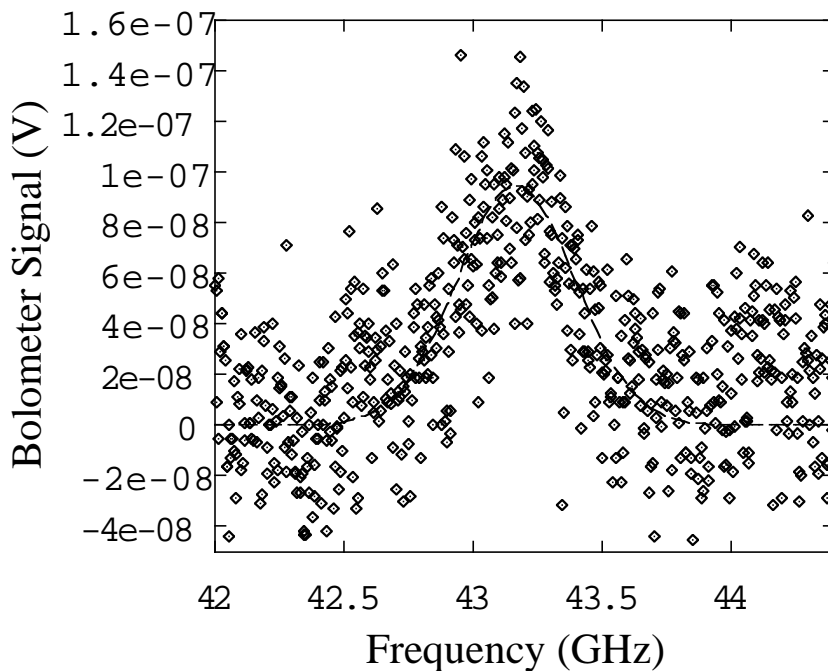


Figure 3.5: Pure rotational spectrum of  $\text{CH}_3\text{F}$ . The best fit to a Gaussian, which determines the center frequency to be 43.1(8) GHz, is shown as a solid line. The resolution is 0.002 GHz.

assuming that the depletion signal is limited by the relaxation rate (see section 1.3.3). When all these factors are taken into account (dipole moment, photon energy, and spin statistics), a maximum signal of about  $0.1 \mu\text{V}$  (from the experimental value of  $1.0 \mu\text{V}$  of signal for HCN) is expected.

Figure 3.5 presents the microwave spectrum of  $\text{CH}_3\text{F}$  observed around 43 GHz. The width of the resonance is about 500 MHz, which is similar to that of HCN, so the  $0.1 \mu\text{V}$  of signal is comparable to the estimate calculated above. Similarly, in the case of  $\text{CD}_3\text{F}$ , shown on Fig. 3.6, the spectrum observed around 36 GHz is also  $\sim 500$  MHz wide, and the signal magnitude is comparable. In both cases, very strong noise is observed, even with long integration times on the lock-in amplifier, and significant oversampling. This is different from the HCN and DCN

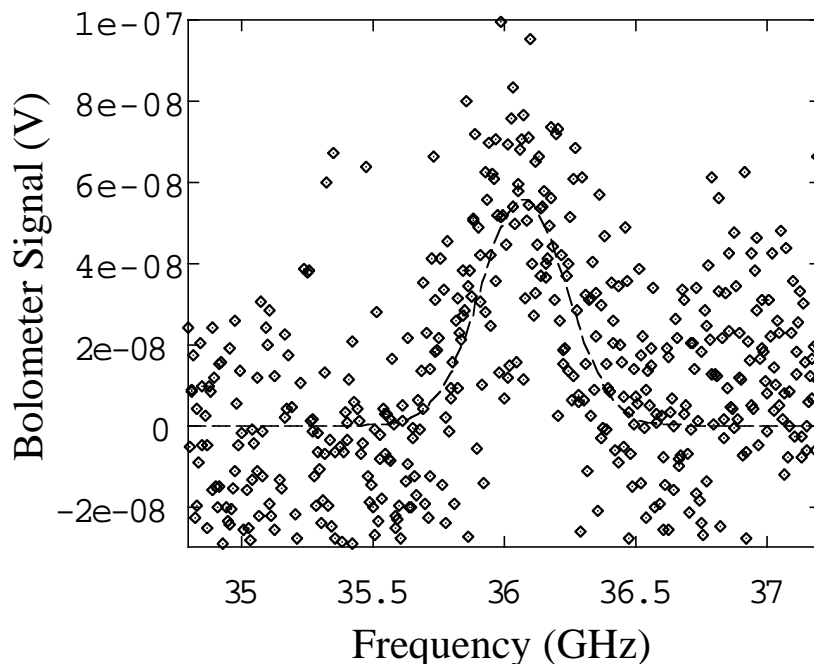


Figure 3.6: Pure rotational spectrum of  $\text{CD}_3\text{F}$ . Shown in solid line is the best fit to a Gaussian, which determines the center frequency to be 36.0(7) GHz. The resolution is 0.005 GHz.

spectra, which feature a signal-to-noise ratio at least an order of magnitude higher.

Unlike the cyanides, where incompletely resolved structure forced the assignment of the transition frequency to the main feature of the resonance signal, the position of the fluorides lines can be determined without ambiguity. As we expect the dominating broadening mechanism to be inhomogeneous [33, 34, 83], the lines were fit to Gaussians, and from the best fit values, the moments of inertia were calculated. The results are shown in Table 3.3. The resonant frequencies were observed around 40 GHz (43.2 GHz for  $\text{CH}_3\text{F}$ , and 36.1 GHz for  $\text{CD}_3\text{F}$ ). These values imply a reduction of the rotational constant, with respect to the gas phase value, of less than 10%. This is what one would expect for fast rotors. However, since these molecules have “intermediate” gas phase rotational constants, the interpretation

Transition		$I_m$	$I_{\text{eff}}$	$I_{\text{eff}} - I_m$
$J = 0 \rightarrow 1$	CH <sub>3</sub> F	19.795	23.4	3.6
	CD <sub>3</sub> F	24.718	28.0	3.3
$J = 1 \rightarrow 2$	CH <sub>3</sub> F	19.795	46.8	27.0
	CD <sub>3</sub> F	24.718	56.0	31.3

Table 3.3: Moments of inertia of CH<sub>3</sub>F and CD<sub>3</sub>F as free molecules ( $I_m$ ) or solvated in <sup>4</sup>He ( $I_{\text{eff}}$ ). Units are amu·Å<sup>2</sup>. The  $J = 0 \rightarrow 1$  transition implies that the fastest of the two rotors sees its moment of inertia reduced the most, the opposite of what is predicted by the theory of the breakdown of the adiabatic following approximation, whereas the  $J = 1 \rightarrow 2$  transition follows the opposite trend.

of the data might not be that simple. The fact that two rotational states remain equally populated at the temperature of the helium droplet, due to spin statistics, guarantees the possibility of observing *two* transitions:  $J=0 \rightarrow 1$  and  $J=1 \rightarrow 2$ . As the effective moment of inertia of these species is not known at present (HENDI infrared experiments have not been performed so far), both possibilities are equally likely.

To identify the nature of the transition, an experiment designed to detect the possible presence of a resonance around 20 GHz has been performed. Using a Hewlett–Packard 8350B/83595A microwave generator [88], and a DBS Microwave active doubler–amplifier [89], up to +20 dBm (100 mW) of microwave power was generated in the region 18–26.5 GHz. No signal was observed, which leads to the conclusion that the transitions around 40 GHz correspond to the  $J=0 \rightarrow 1$  resonance. However, the magnitude of the noise in this last series of experiment (20 GHz) was even more intense, which prevented us from *definitely* assigning the observed transition as the  $J=0 \rightarrow 1$ . Nevertheless, it is possible to justify the choice of the transition originating from  $J=0$ , instead of  $J=1$ ; the reasons will be presented below.

The values of the effective moment of inertia show that the slowest of the

two rotors features the smallest change induced by the helium. At first sight, this conclusion seems contradictory to the theory of the breakdown of the adiabatic following approximation presented in Sec. 3.2.  $\text{CH}_3\text{F}$ , which is faster than  $\text{CD}_3\text{F}$  by about 20% (in the gas phase), shows an increase of its moment of inertia 10% larger than that of  $\text{CD}_3\text{F}$ . The opposite situation was predicted, based exclusively on the rotational velocity of the rotors. The effect of “dynamic sphericity” was mentioned earlier, and although its effect in the case of HCN and DCN has not been observed, it might be of importance in the present case. For the methyl-like molecules studied here, full deuteration involves a change of mass of three amu, over a total mass of 34 amu (about 9%), whereas in the case of the cyanides, the change was of only one amu over a molecular mass of 29 amu (about 3%). This effect may fully compensate for the hydrodynamic drag and cause the largest change in moment of inertia to the lightest rotor (the less spherical), especially in this case, where the molecules are not truly “fast” rotors, and the breakdown of the adiabatic following is not expected to be as dramatic as in the case of HCN and DCN. The effect of the displacement of the center of mass for  $\text{CH}_3\text{F}$  and  $\text{CD}_3\text{F}$  will be addressed in the remainder of this chapter.

According to Ref. 4 (see equation 74 on page 664), the hydrodynamic contribution to the increase of moment of inertia ( $\Delta I_B$ ) of an ellipsoid rotating perpendicularly to its symmetry axis can be written as:

$$\Delta I_B = I' \cdot \Delta(\xi) + M' \gamma_1 r_{\text{com}}^2 \quad (3.4)$$

where  $I'$  is the value of the moment of inertia for the ellipsoid if filled with helium,  $M'$  is the mass of helium displaced by the ellipsoid, and  $\Delta(\xi)$  is the “hydrodynamic

constant” of the rotor

$$I' = \frac{1}{5}M'a^2(1 + \xi^2) \quad (3.5)$$

$$M' = M_{\text{He}}\rho\frac{4}{3}\pi a^3\xi \quad (3.6)$$

$$\Delta(\xi) = \frac{1}{1 + \xi^2} \frac{(1 - \xi^2)^2(\alpha_0 - \gamma_0)}{2(1 - \xi^2)^2 - (1 + \xi^2)(\alpha_0 - \gamma_0)} \quad (3.7)$$

The ellipsoid has a length  $\xi a$  ( $\xi$  is the ratio of the length of both axis: for a sphere,  $\xi = 1$ ). The helium droplet is considered to have a uniform density  $\rho = 0.022$  atoms/ $\text{\AA}^3$ , and a mass  $M_{\text{He}} = 4$  amu. The terms  $\alpha_0$ ,  $\gamma_0$ ,  $\alpha_1$ , and  $\gamma_1$  are contributions to the classical kinetic energy of translational motion of the ellipsoid (see Ref. 4 for more details). The size of the ellipsoids were estimated from the He-impurity pair potentials calculated at the MP4 level [90]. The “long” axis ( $\xi a$ ) is set to the sum of the distances between the center of mass of the molecule and the inner wall at  $0^\circ$  and  $180^\circ$ . The short axis ( $a$ ) is set to twice the distance between the center of mass and the inner wall, calculated at  $90^\circ$ . The values  $a = 6.4$   $\text{\AA}$  and  $\xi = 1.03$   $\text{\AA}$  (for a long axis of  $\xi a = 6.6$   $\text{\AA}$ ) were obtained. For  $\xi \approx 1$ , equation 3.7 can be approximated by the expansion  $\Delta(\xi) \approx \frac{2}{3}(\xi - 1)^2$ . We get  $\Delta(\xi) = 6 \times 10^{-4}$ ,  $M' = 99.53$ , and  $I' = 1680.4$ .  $\gamma_1$  can be estimated to be 0.6 (from figure 8 of reference 4).

For both  $\text{CH}_3\text{F}$  and  $\text{CD}_3\text{F}$ , the first term of equation 3.4,  $I' \cdot \Delta(\xi)$ , will have the same value, as it only depends upon the size of the ellipsoid ( $a$ , and  $\xi$ ) and the properties of the helium droplet ( $M'$ ). Using the equations above, we get  $I' \cdot \Delta(\xi) = 1.0$ . The second term, however, is a function of the distance between the center of rotation and the center of mass of the ellipsoid, and we expect to get a different value for both molecules.

The term  $r_{\text{com}}^2$  is easily calculated from the bond lengths and angles of  $\text{CH}_3\text{F}$ . In the present work, the value for  $\text{CD}_3\text{F}$  is obtained from the  $\text{CH}_3\text{F}$  parameters, and only the masses were changed. For C–H and C–F bond lengths of respectively 1.095 and 1.382 Å, and a H–C–H angle of  $110.45^\circ$ , one gets that  $r_{\text{com}}^2 = 0.1586 \text{ \AA}^2$  for  $\text{CH}_3\text{F}$ , and  $0.0777 \text{ \AA}^2$  for  $\text{CD}_3\text{F}$ . From these values, we get that the second term in equation 3.4,  $M'\gamma_1 r_{\text{com}}^2$ , is equal to 9.47 for  $\text{CH}_3\text{F}$ , and 4.64 for  $\text{CD}_3\text{F}$ , for a total change of moment of inertia of 10.47 for  $\text{CH}_3\text{F}$ , and 5.64 for  $\text{CD}_3\text{F}$ . Recall the experimental values (see table 3.3) of 3.6 for  $\text{CH}_3\text{F}$ , and 3.3 for  $\text{CD}_3\text{F}$ . The calculated variation of moment of inertia is substantially larger than the experimental value: Considering  $\text{CH}_3\text{F}$  and  $\text{CD}_3\text{F}$  to be ellipsoidal, instead of pear-shaped, is obviously a rather crude approximation. Neglecting the spatial dependence of the helium density  $\rho$  around the impurity is also known to lead to incorrect results [6]. Nevertheless, the preceding calculation confirms that the effect of the displacement of the center of mass cannot be neglected in the case of the methyl fluorides. Fully three-dimensional simulations that take into account both the radial dependence of the helium density (see Ref. 6), and the irregular shape of these molecules would provide essential information regarding the relaxation of these “not-so-fast” rotors in helium nanodroplets.

# Conclusions

The work presented in this dissertation has addressed two important issues concerning the relaxation of molecular species embedded in helium nanodroplets. Firstly, the ability to form and spectroscopically interrogate free radicals was discussed. The  $\text{NO}_2$  experiment showed that nonradiative cooling plays a major role in the dynamics, as the dissociation of the molecule is suppressed, up to excess energies reaching  $2000 \text{ cm}^{-1}$ . The beam depletion results provided evidence that, over all the energy region surveyed,  $25\,000$  to  $27\,147 \text{ cm}^{-1}$ , a constant fraction of the photon energy is relaxed in the helium bath upon excitation. The absence of fluorescence from the embedded species, from both below and above the dissociation threshold, allowed the calculation of an upper limit of  $90 \text{ ns}$  for the nonradiative relaxation timescale. The experimental data is compatible with three of the four different relaxation mechanisms that were proposed. Only the presence (or absence) of the dissociation products  $\text{O}$  and  $\text{NO}$ , prior to recombination followed by fast nonradiative decay, will lead to the identification of the true relaxation pathway. The feasibility of detecting the  $\text{NO}$  radical *via* one- and two-photon excitation at  $\sim 200 \text{ nm}$  was discussed.

Secondly, the pure rotational spectra of two pairs of isotopomers,  $\text{HCN}/\text{DCN}$  and  $\text{CH}_3\text{F}/\text{CD}_3\text{F}$ , were recorded. From the observed microwave resonances, the effective moments of inertia of the rotors (the moment of inertia altered by the interac-

tion with the superfluid bath) were calculated. Contrary to the adiabatic following approximation of the hydrodynamic model, it was found that both rotors of a given pair were not affected by helium the same way. In the case of HCN and DCN, where both molecules fall in the “fast rotors” regime, the faster of the two (HCN, by 23% in the gas phase) sees its moment of inertia less affected (by 9%) by the helium environment. This is considered a direct observation of the failure of the adiabatic following approximation, which states that the helium density adiabatically follows the motion of the embedded impurities. For  $\text{CH}_3\text{F}$  and  $\text{CD}_3\text{F}$ , the opposite trend is observed, and the moment of inertia of  $\text{CH}_3\text{F}$  (the faster of the two rotors, by 20% in the gas phase) is increased 10% more than that of  $\text{CD}_3\text{F}$ . A simple calculation of the hydrodynamic contribution to the increase of moment of inertia suggested that “dynamical sphericity”, which is greatly affected by isotopic substitution, may play an important role in the relaxation process of these methyl-like rotors. Further theoretical work is needed to obtain quantitative evidence.

WHERE DO I BEGIN ... ON THE HEELS OF RIMBAUD MOVING  
LIKE A DANCING BULLET THRU THE SECRET STREETS OF  
A HOT NEW JERSEY NIGHT FILLED WITH VENOM AND WONDER.  
MEETING THE QUEEN ANGEL IN THE REEDS OF BABYLON AND  
THEN TO THE FOUNTAIN OF SORROW TO DRIFT AWAY IN  
THE HOT MASS OF THE DELUGE ... TO SING PRAISE TO THE  
KING OF THOSE DEAD STREETS, TO GRASP AND LET GO IN  
A HEAVENLY WAY – STREAMING INTO THE LOST BELLY OF  
CIVILIZATION AT A STAND STILL. ROMANCE IS TAKING OVER  
TOLSTOY WAS RIGHT. THESE NOTES ARE BEING WRITTEN IN  
A BATHTUB IN MAINE UNDER IDEAL CONDITIONS, IN EVERY  
CURIO LOUNGE FROM BROOKLYN TO GUAM, FROM LOWELL TO  
DURANGO OH SISTER, WHEN I FALL INTO YOUR  
SPACY ARMS, CAN NOT YA FEEL THE WEIGHT OF OBLIVION  
AND THE SONGS OF REDEMPTION ON YOUR BACKSIDE WE  
SURFACE ALONGSIDE MILES STANDISH AND TAKE THE ROCK.  
WE HAVE RELATIONS IN MOZAMBIQUE. I HAVE A BROTHER  
OR TWO AND A WHOLE LOT OF KARMA TO BURN ... ISIS AND  
THE MOON SHINE ON ME. WHEN RUBIN GETS OUT OF JAIL,  
WE CELEBRATE IN THE HISTORICAL PARKING LOT IN SUNBURNED  
CALIFORNIA ...

*Bob Dylan, 1975*

# Bibliography

- [1] S. Goyal, D.L. Schutt, and G. Scoles. *Phys. Rev. Lett.*, 69:933, 1992.
- [2] S. Goyal, D.L. Schutt, and G. Scoles. *J. Phys. Chem.*, 97:2236, 1993.
- [3] J. Reho, U. Merker, M.R. Radcliff, K.K. Lehmann, and G. Scoles. *J. Chem. Phys.*, 112:8409, 2000.
- [4] K.K. Lehmann. *Mol. Phys.*, 97:645, 1999.
- [5] E. Lee, D. Farrelly, and K.B. Whaley. *Phys. Rev. Lett.*, 83:3812, 1999.
- [6] C. Callegari, A. Conjusteau, I. Reinhard, K.K. Lehmann, G. Scoles, and F. Dalfovo. *Phys. Rev. Lett.*, 83:5058, 1999; 84:1848(E), 2000.
- [7] E. Whittle, D.A. Dows, and G.C. Pimentel. *J. Chem. Phys.*, 22:1943, 1954.
- [8] L. Vegard. *Nature*, 114:357, 1924.
- [9] D.E. Milligan and M.E. Jacox. *J. Chem. Phys.*, 38:2627, 1963.
- [10] D.E. Milligan and M.E. Jacox. *J. Chem. Phys.*, 39:712, 1963.
- [11] T.E. Gough, D.G. Knight, and G. Scoles. *Chem. Phys. Lett.*, 97:155, 1983.
- [12] T.E. Gough, M. Mengel, P.A. Rowntree, and G. Scoles. *J. Chem. Phys.*, 83:4958, 1985.
- [13] A. Schneidemann, J.P. Toennies, and J.A. Northby. *Phys. Rev. Lett.*, 64:1899, 1990.
- [14] M. Hartmann, R.E. Miller, J.P. Toennies, and A. Vilesov. *Phys. Rev. Lett.*, 75:1566, 1995.

- [15] D.M. Brink and S. Stringari. *Z. Phys. D*, 15:257, 1990.
- [16] J. Gspann. In S. Datz, editor, *Physics of Electronic and Atomic Collisions*, page 79. North Holland, Amsterdam, 1992. ; D.M. Brink and S. Stringari, *Z. Phys. D*, 15:257, 1990.
- [17] S. Grebenev, J.P. Toennies, and A.F. Vilesov. *Science*, 279:2083, 1998.
- [18] P. Sindzingre, M.L. Klein, and D.M. Ceperley. *Phys. Rev. Lett.*, 63:1601, 1989.
- [19] A. Conjusteau, C. Callegari, I. Reinhard, K.K. Lehmann, and G. Scoles. *J. Chem. Phys.*, 113:4840, 2000.
- [20] C. Callegari, A. Conjusteau, I. Reinhard, K.K. Lehmann, and G. Scoles. *J. Chem. Phys.*, 113:10535, 2000.
- [21] Carlo Callegari. *Molecular Rotation and Dynamics in Superfluid  $^4\text{He}$  Nanodroplets*. PhD thesis, Princeton University, 2000.
- [22] K.B. Whaley. In J.M. Bowman and Z. Bacic, editors, *Advances in Molecular Vibrations and Collision Dynamics*, page 397. JAI Press, 1998.
- [23] S.A. Chin and E. Krotscheck. *Phys. Rev. B*, 52:10405, 1995.
- [24] J. Higgins, C. Callegari, J.H. Reho, F. Stienkemeier, W.E. Ernst, K.K. Lehmann, M. Gutowski, and G. Scoles. *Science*, 273:629, 1996.
- [25] K. Nauta and R.E. Miller. *Science*, 283:1895, 1999.
- [26] K. Nauta and R.E. Miller. *Farad. Discuss.*, 113:261, 1999.
- [27] K. Nauta and R.E. Miller. *Science*, 287:293, 2000.
- [28] K. Liu, M.G. Brown, and R.J. Saykally. *J. Phys. Chem.*, 101:8995, 1997.
- [29] Lakeshore Cryotronics, Pre-Cooler: Temperature Controller model 320; Nozzle: Temperature Controller model 321.  
<http://www.lakeshore.com>.
- [30] E.L. Knuth, B. Schilling, and J.P. Toennies. In *19<sup>th</sup> International Symposium on Rarefied Gas Dynamics, University of Oxford, 1994*. Oxford University Press, Oxford, 1995.
- [31] R.A. Smith, T. Ditmire, and J.W.G. Tisch. *Rev. Sci. Inst.*, 69:3798, 1998.

- [32] M. Lewerenz, B. Schilling, and J.P. Toennies. *Chem. Phys. Lett.*, 206:381, 1993.
- [33] I. Reinhard, C. Callegari, A. Conjusteau, K.K. Lehmann, and G. Scoles. *Phys. Rev. Lett.*, 82:5036, 1999.
- [34] C. Callegari, I. Reinhard, K.K. Lehmann, G. Scoles, K. Nauta, and R.E. Miller. *J. Chem. Phys.*, 113:4636, 2000.
- [35] J. Reho, J. Higgins, C. Callegari, K.K. Lehmann, and G. Scoles. *J. Chem. Phys.*, 113:9686, 2000.
- [36] J. Reho, J. Higgins, K.K. Lehmann, and G. Scoles. *J. Chem. Phys.*, 113:9694, 2000.
- [37] Beam Dynamics, Inc., model 1, 0.4 mm nominal (0.380 mm measured).  
<http://www.beamdynamicsinc.com>.
- [38] Infrared Laboratories, silicon bolometer, unit #1754.  
<http://www.irlabs.com>.
- [39] Infrared Laboratories, JFET Preamplifier Cold Module Model #LN-6C.  
<http://www.irlabs.com>.
- [40] FETs have a transconductance  $g$  (function of the drain current  $i_d$  and gate-source voltage drop  $v_{gs}$ ) defined as  $g = i_d/v_{gs}$ . The output impedance  $Z_{\text{out}}$  of such devices is defined as the reciprocal of the transconductance. Thus, for the circuit shown, the output impedance is  $R_{\text{out}} = \frac{1}{g} \parallel R_s$ , where  $\frac{1}{g}$  is about 500  $\Omega$ , and  $R_s$  is 12 k $\Omega$ , for  $R_{\text{out}} = 480 \Omega$ . See P. Horowitz, and W. Hill, *The Art of Electronics*, 2<sup>nd</sup> Ed., Cambridge University Press, 1989.
- [41] Stanford Instruments, SR510 single-phase analog lock-in amplifier.  
<http://www.srsys.com>.
- [42] Stanford Instruments, SR550 FET inputs low noise preamplifier.  
<http://www.srsys.com>.
- [43] SPI Supplies, Platinum disc with 10 $\mu\text{m}$  aperture.  
<http://www.spi.cc>.
- [44] G. Scoles, editor. *Atomic and Molecular Beam Methods*. Oxford University Press, Inc., 1988.
- [45] David Chandler. *Introduction to Modern Statistical Mechanics*. Oxford Univer-

- sity Press, Inc., 1987.
- [46] Pre-Cooler: CTI Vacuum CP22, up to 1 W at 20 K; Nozzle: CTI Vacuum 350CP, up to 4 W at 20 K.  
<http://www.ctivacuum.com>.
- [47] Luxél Radak II furnace, with Radak II power supply (featuring a Eurotherm 2404 temperature controller).  
<http://www.luxel.com>.
- [48] Fractballs. 1 mm in diameter, 92.8 % alumina, density of 1.1 g/cm<sup>3</sup> and porosity of 70 %, for an effective surface area of 1240 cm<sup>2</sup>/g, maximum temperature of 1900 °C.  
<http://www.buyrefractory.com>.
- [49] C.J. O'Brien. *Improvements to an infrared laser-molecular beam spectrometer for IVR studies*. Senior's Thesis, Princeton University, 1994.
- [50] Infrared Laboratories, composite bolometer, unit #1346.  
<http://www.irlabs.com>.
- [51] Positive Light.  
<http://www.poslight.com>.
- [52] Roman Schmied. *Superfluidity in Small para-Hydrogen Clusters: A Molecular Beam – Laser Setup for Raman Spectroscopy*. Travail pratique de diplôme d'Ingénieur Physicien, EPFL, 2001.
- [53] John P. Higgins. *Cluster Isolation Spectroscopy*. PhD thesis, Princeton University, 1998.
- [54] James H. Reho. *Time-Resolved Spectroscopy of Atomic and Molecular Dopants In and On Helium Nanodroplets*. PhD thesis, Princeton University, 2000.
- [55] Andover Corp., Long pass filter glass, item #435G03-50.  
<http://www.andcorp.com>.
- [56] Hamamatsu Photosensor Module model #5783-03.  
<http://www.hamamatsu.com>.
- [57] Burle Electron Tubes, model 8853 12 stages Quantacon photomultiplier.
- [58] Newport Corp. UV fused silica lens, item #SPX022, with AR.10 broadband

UV anti-reflection coating.

<http://www.newport.com>.

- [59] Ira N. Levine. *Molecular Spectroscopy*. Wiley, 1975.
- [60] I. Bezel, P. Ionov, and C. Wittig. *J. Chem. Phys.*, 111:9267, 1999.
- [61] B.S. Jursic. *J. Mol. Struct.-Theochem*, 492:85, 1999.
- [62] B.S. Jursic. *J. Phys. Chem. A*, 103:5773, 1999.
- [63] B.S. Jursic. *J. Mol. Struct.-Theochem*, 499:91, 2000.
- [64] E. Culotta and D.E. Koshland Jr. *Science*, 258:1862, 1992.
- [65] R. Jost, J. Nygård, A. Pasinski, and A. Delon. *J. Chem. Phys.*, 105:1287, 1996.
- [66] G.D. Gillispie, A.V. Khan, A.C. Wahl, R.P. Hosteny, and M. Krauss. *J. Chem. Phys.*, 63:3425, 1975.
- [67] J. Miyawaki, K. Yamanouchi, and S. Tsuchiya. *J. Chem. Phys.*, 101:4505, 1994.
- [68] A. Delon, F. Reiche, B. Abel, S.Y. Grebenschikov, and R. Schinke. *J. Phys. Chem. A*, 104, 2000.
- [69] N. Shafisadeh, P. Brechignac, M. Dyngaard, J.H. Fillion, D. Gauyacq, J.C. Miller, T Pino, and M. Raoult. *J. Chem. Phys.*, 108, 1998.
- [70] A. Delon, S. Heilliette, and R. Jost. *Chem. Phys.*, 238:465, 1998.
- [71] D.M. Wardlaw and R.A. Marcus. *J. Chem. Phys.*, 83:3462, 1985.
- [72] R.C. Weast. *CRC Handbook of Chemistry and Physics*. CRC Press, Inc., 1989–1990.
- [73] One of the leads got partially detached from the diamond plate, thus the enormous contact noise when cooled to 1.6 K (the contact tested perfectly fine at room temperature, as the problem was due to contraction upon cooling).
- [74] J. Luque and D.R. Crosley. *J. Chem. Phys.*, 16:7405, 1999.
- [75] J. Burris, T.J. Mcgee, and T.J. McIlrath. *Chem. Phys. Lett*, 101:588, 1983.
- [76] R.J. Hochstrasser, G.R. Meredith, and H.P. Trommsdorf. *Chem. Phys. Lett.*, 53:423, 1978.

- [77] J. Harms, M. Hartmann, J.P. Toennies, A.F. Vilesov, and B. Sartakov. *J. Mol. Spec.*, 185:204, 1997.
- [78] K. Nauta and R.E. Miller. *J. Chem. Phys.*, 111:3426, 1999.
- [79] Y. Kwon and K.B. Whaley. *Phys. Rev. Lett.*, 83:4108, 1999.
- [80] R. Fröchtenicht, M. Kaloudis, M. Koch, and F. Huisken. *J. Chem. Phys.*, 105:6128, 1996.
- [81] M. Behrens, U. Buck, R. Fröchtenicht, M. Hartmann, F. Huisken, and F. Rohmund. *J. Chem. Phys.*, 109:5914, 1998.
- [82] K. Nauta and R.E. Miller. *Phys. Rev. Lett.*, 82:4480, 1999.
- [83] K. Nauta and R.E. Miller. *J. Chem. Phys.*, 113:9466, 2000.
- [84] The formula used (in MKS units) is:  $T_1 T_2 = (1/2)\epsilon_0 \hbar^2 c / [(1/3)\mu^2 I_s]$ , where  $\mu$  is the electrical dipole moment of the molecule, and  $I_s$  is the saturation intensity (see, *e. g.*, A. Yariv, *Quantum Electronics*, John Wiley & Sons, Inc., New York, 1975, Chapter 8).
- [85] K.M. Atkins and J.M. Hutson. *J. Chem. Phys.*, 105:440, 1996.
- [86] Erik W. Draeger. *Path Integral Monte Carlo Simulations of Helium: From Superfluid Droplets to Quantum Crystals*. PhD thesis, University of Illinois at Urbana-Champaign, 2001.
- [87] M.S. Cord, J.D. Petersen, M.S. Lojko, and R.H. Haas. *Microwave Spectral Tables, Volume IV. Polyatomic Molecules Without Internal Rotation*. U.S. National Bureau of Standards, 1968.
- [88] Hewlett Packard Corp., model #8350B synthesiser with #83595A power plugin. Now Agilent Technologies.
- [89] DBS Microwave, model #DBS-1826x220. Minimum input power +10 dBm at 9.0–13.25 GHz, maximum output power: +20 dBm at 18–26.5 GHz. <http://www.dbsmw.com>.
- [90] K. Higgins, Private communication.